Contrib Mineral Petrol (1998) 130: 358–378

John M. Ferry · Sorena S. Sorensen
Douglas Rumble III

Structurally controlled fluid flow during contact metamorphism in the Ritter Range pendant, California, USA

Received: 27 January 1997 / Accepted: 2 October 1997

Abstract The mineralogy and O-isotope geochemistry of siliceous limestones from the Ritter Range pendant constrain the geometry and amount of fluid flow during contact metamorphism associated with emplacement of a pluton of the Sierra Nevada Batholith. Wollastonite (Wo) replaces calcite (Cal) + quartz (Qtz) on a layer-by-layer basis in homoclinal beds that strike NW and dip almost vertically. At the peak of metamorphism ($P \approx 1500$ bars, $T \approx 600$ °C) fluid in equilibrium with Cal, Qtz, and Wo has composition $X_{CO_2} = 0.28$, requiring that the Wo-forming reaction was driven by infiltration of reactive H_2O-rich fluid. The spatial distribution of Wo and Cal + Qtz records that peak metamorphic fluid flow was layer-parallel, upward. Bounds on the prograde time-integrated fluid flux associated with formation of Wo are set by: (1) the overlap in O-isotope composition between Wo-bearing and Wo-free rocks (>245 mol fluid/cm^2 rock); (2) the amount of fluid that would drive the Wo-reaction front upward to the present level of exposure from a point at depth where Cal, Qtz, and Wo would be in equilibrium with pure CO_2 (<1615 mol/cm^2). Back-reaction of Wo to Cal + Qtz records an additional time-integrated retrograde fluid flux of ≈200–1000 mol/cm^2. The direction and amount of flow inferred from mineralogical and isotopic data agree with the results of the hydrologic model for metamorphic fluid flow in the area of Hanson et al. (1993). Fingers of Wo-bearing rock that extend farthest from the fluid source along contacts between limestone and more siliceous rocks point to strong control of flow geometry at the 0.1–100 m scale exerted by premetamorphic structures. Studies that neglect structural control at this scale may fail to predict correctly fundamental aspects of contact metamorphic fluid flow.

J.M. Ferry (✉)
Department of Earth and Planetary Sciences,
Johns Hopkins University, Baltimore, MD 21218, USA
e-mail: jferry@jhu.edu

S.S. Sorensen
Department of Mineral Sciences, NHB-119,
National Museum of Natural History,
Smithsonian Institution, Washington, DC 20560, USA

D. Rumble III
Geophysical Laboratory, 5251 Broad Branch Road,
NW Washington, DC 20015, USA

Editorial responsibility: T.L. Grove

Introduction

Fluid infiltration can control both the mineralogical and stable isotopic composition of rocks during contact metamorphism (e.g., Nabelek et al. 1984; Labotka et al. 1988; Heinrich and Gottschalk 1994). Two approaches used to constrain the geometry and amount of contact metamorphic fluid flow are based on: (1) the distribution of mineral assemblages and stable isotopic compositions of metamorphosed rocks (Jamtveit et al. 1992; Bowman et al. 1994; Dipple and Ferry 1996); (2) thermal and hydrologic models of hydrothermal systems around cooling plutons (e.g., Norton and Knight 1977; Hanson 1995a; Gerdes et al. 1995a). Different predictions made by the two methods have led to debate over the amount and direction of fluid flow in contact aureoles (e.g., Ferry 1995a; Hanson 1995b). This investigation of contact metamorphism in the Ritter Range pendant, central Sierra Nevada, California, contributes to a resolution of the debate. Flow of chemically reactive fluids through siliceous carbonate rocks during metamorphism produced wollastonite from calcite and quartz. The pathways of metamorphic fluid flow are easily imaged in the field from the distribution of distinctive-looking wollastonite-bearing rocks. Because of topographic relief and good exposure in the Ritter Range pendant, the geometry of the metamorphic fluid flow system therefore could be mapped in three dimensions. The distribution and amount of wollastonite can be simply interpreted with transport theory in terms of the direction and amount of fluid flow. Estimates of the direction and

amount of fluid flow based on mineralogical and stable isotopic data agree, within error, with independent estimates from the thermal-hydrologic model of Hanson et al. (1993) for the same area.

Geologic setting

The Ritter Range is one of the largest roof pendants in the Sierra Nevada Batholith (≈600 km^2). This study involved a small portion of the pendant that has been mapped at a scale of 1:6000 (Fig. 1; Fiske and Tobisch 1978; unpublished maps by R.S. Fiske and O.T. Tobisch). Hanson et al. (1993) summarize the geologic setting. Briefly, most of the study area is underlain by Triassic to Upper Jurassic or lowermost Cretaceous metamorphosed basaltic to rhyolitic lavas and pyroclastic and volcaniclastic rocks. Minor beds of pelite and siliceous carbonate rock are interlayered with the metavolcanic rocks. Carbonate layers typically are a few m thick or less but may range to 30 m. Although some thick metavolcanic units span the study area (Fig. 1), thinner units pinch out along strike over distances of several 10s to several 100s m.

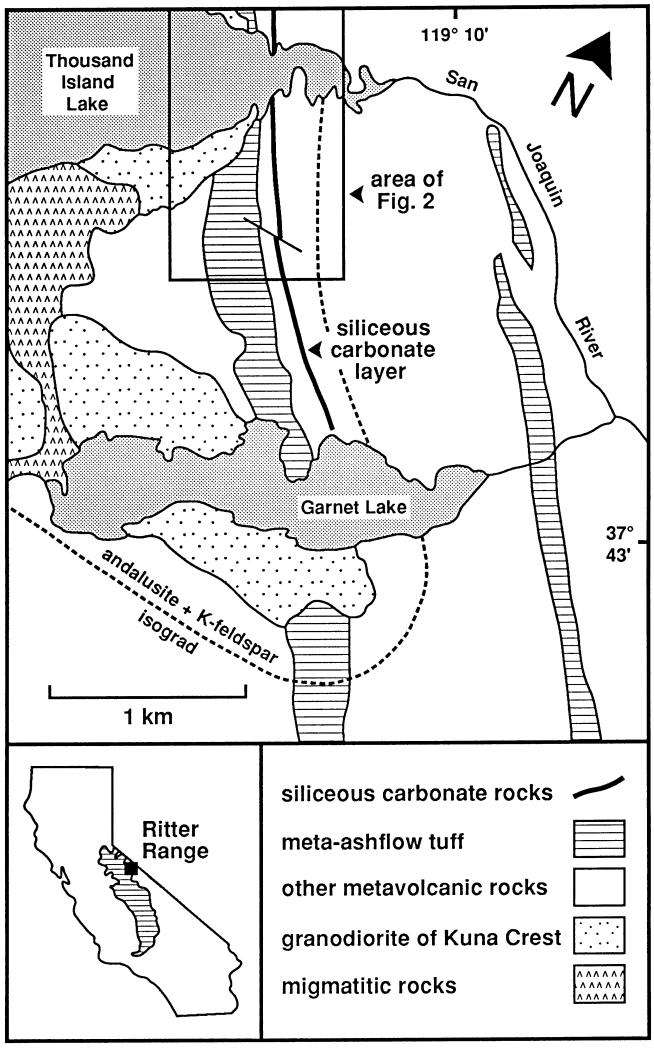

Fig. 1 Geologic sketch map of the part of the Ritter Range pendant considered in this study (after Hanson et al. 1993). *Inset* shows location of the pendant relative to the exposure of the Sierra Nevada Batholith. Area of granodiorite at Garnet Lake includes a migmatitic border zone up to ≈100 m wide

Lithologic layering is homoclinal in the study area (Fig. 2); layers strike NW and dip steeply to the SW. Stratigraphy faces upward to the SW. Penetrative foliation is either parallel or at a small angle to lithologic layering. Layers are dramatically thinned by flattening parallel to bedding with estimated strain ≈50% (Tobisch et al. 1977; Tobisch and Fiske 1982). Some lithologic layering is discontinuous at the 10–100 m scale because of boudinage associated with the flattening. The stratigraphy in the area of Fig. 1 is probably repeated by low-angle faults, although their precise location has proven difficult to determine.

The study area is intruded by the ≈91 Ma granodiorite of Kuna Crest (Stern et al. 1981), the oldest phase of the Tuolomne intrusive series. The exposures of granodiorite in Fig. 1 may be connected at depth. Intrusion of the granodiorite caused hornblende-hornfels- to pyroxene-hornfels-facies contact metamorphism. The metamorphic gradient is expressed by the andalusite + K-feldspar isograd in Fig. 1 mapped from mineral assemblages in metamorphosed pelites and rhyolites. Some porphyroblasts are boudinaged and define penetrative foliation whereas others cross-cut the foliation and exhibit no preferred orientation. The growth of peak metamorphic minerals therefore coincided with and outlasted the deformation.

Following deposition but prior to Cretaceous contact metamorphism, the volcanic rocks experienced significant metasomatic increases in K- and/or Na-contents and $^{18}O/^{16}O$, local enrichment in Mn and Mg, and oxidation (Hanson et al. 1993; Sorensen et al. in press). The mineralogical effects of contact metamorphism discussed in this report are unrelated to the earlier metasomatic effects.

This study focused on a single 30–50-m-thick layer of siliceous carbonate rock (Fig. 1). The layer, which extends NW of the boundary of the map area and terminates just NW of Garnet Lake, was examined in detail at 4 locations (Fig. 2). Lithologic layering strikes 140–150° and dips 75–85° SW. At each location the carbonate layer is bounded on both sides by mafic to intermediate metavolcanic rocks (the lower contact between the carbonate layer and metavolcanic rock is buried under alluvium at location 4). Stratigraphy across 3 of the 4 traverses (locations 1, 2, 4) is qualitatively the same (Figs. 3–6). The base of the layer is composed of calc-silicate hornfels which in turn is overlain by siliceous limestone, siliceous dolomite, and a second siliceous limestone. At location 3 the layer lacks siliceous dolomite and instead displays a 3.4-m-wide band of metavolcanic rock separating the two siliceous limestones. Thickness of these lithologies differs significantly among the locations. Variations in stratigraphy between the locations likely result from a combination of primary differences in layer thickness and the effects of deformation.

Methods of investigation

Forty-four samples of siliceous limestone, siliceous dolomite, and calc-silicate hornfels were collected along traverses perpendicular to layering (Figs. 2–6). As determined from enlarged air photos and a topographic map, the four locations are separated by ≈1.3 km horizontally and ≈95 m vertically. Additional samples were collected from the lower siliceous limestone from a small area ≈50 m NW of the traverse at location 2 (Fig. 7).

Mineral assemblages were identified by optical and scanning electron microscopy of thin sections. Qualitative analyses of all minerals were obtained by energy dispersive spectrometry (EDS) with the JEOL JXA-8600 electron microprobe at Johns Hopkins University. Minerals that showed detectable deviation from ideal compositions were quantitatively analyzed with wavelength dispersive spectrometry using natural silicate and carbonate mineral standards and a ZAF correction scheme (Armstrong 1988). Modes of 21 samples were measured by counting ≥2000 points in a thin section with back-scattered electron imaging. Any uncertainty in the identification of a particular point was resolved by obtaining an

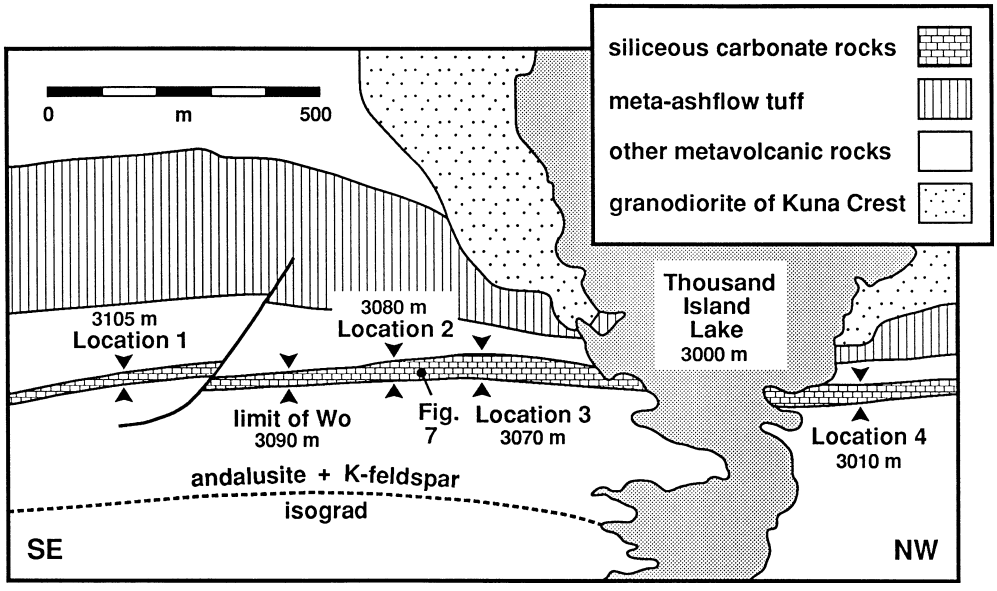

Fig. 2 Enlargement of a portion of Fig. 1 showing the 4 sample locations in the siliceous carbonate layer (after Fiske and Tobisch 1978, and their unpublished maps)

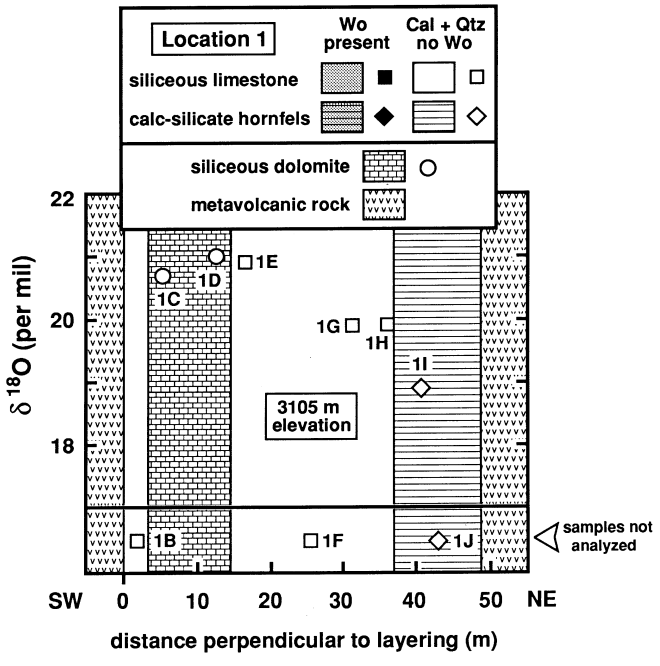

Fig. 3 Lithology and O-isotope composition of the carbonate layer along a traverse perpendicular to strike of lithologic layering at location 1. *Symbols* show where samples were collected whose mineralogy was determined from thin sections. Sample designation the same as in text and tables (*number* refers to location; *letters* increase in alphabetical order along the traverse from SW to NE). The isotopic compositions of samples plotted below the *thick horizontal line* were not measured

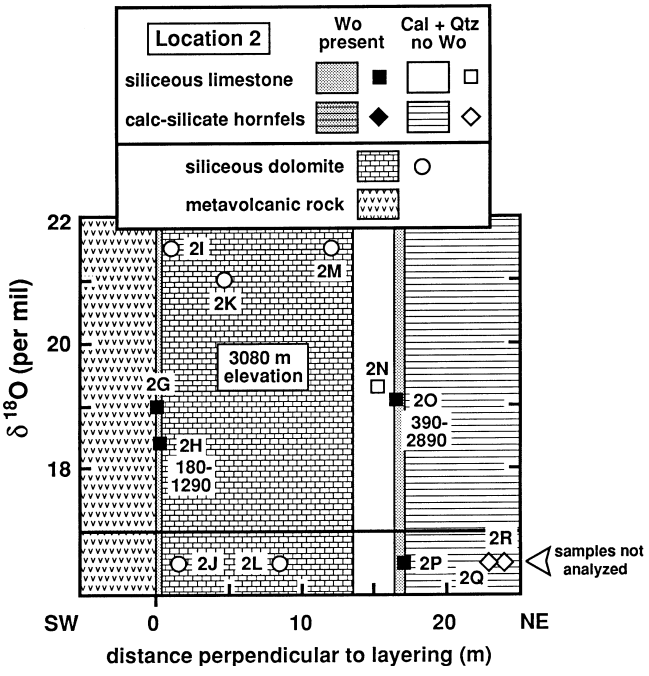

Fig. 4 Lithology and O-isotope composition of the carbonate layer along a traverse perpendicular to strike of lithologic layering at location 2. Range of numbers by sample designations denotes lower and upper bounds on the prograde time-integrated fluid flux associated with formation of Wo by Reaction 1 and Grs by Reaction 2 in moles fluid/cm^2 rock (see text for details). Other features same as in Fig. 3

EDS X-ray spectrum. Modes of selected, representative samples of siliceous limestone, calc-silicate hornfels, and dolomite from the four sample locations are listed in Table 1. Compositions of analyzed minerals in 12 of these samples appear in Table 2.

Calcite from 28 samples was analyzed for oxygen and carbon isotope composition following procedures described by Rumble et al. (1991). Approximately 2–5 mg finely powdered calcite was obtained with a 2 mm, diamond-tipped drill from a polished rock slab. Calcite was dissolved in phosphoric acid (McCrea 1950) in evacuated reaction vessels at 60 °C. Extracted CO_2 was analyzed with the Finnigan MAT 252 mass spectrometer at the Geophysical Laboratory. The acid fractionation factor was computed with the expression in Swart et al. (1991) using their calibration for sealed reaction vessels. Results were normalized to the composition of calcite standard NBS-19 ($\delta^{18}O = 28.65‰$, VSMOW; $\delta^{13}C = 1.95‰$, VPDB, Coplen 1988, 1996). Analysis of NBS-19 and other

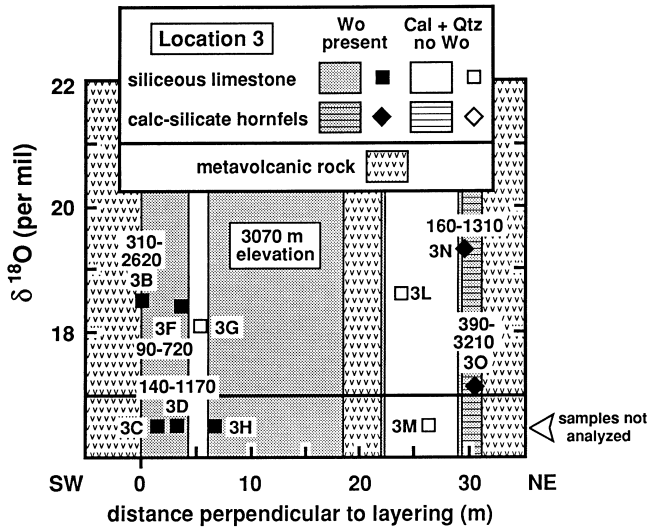

Fig. 5 Lithology and O-isotope composition of the carbonate layer along a traverse perpendicular to strike of lithologic layering at location 3. Other features same as in Figs. 3 and 4

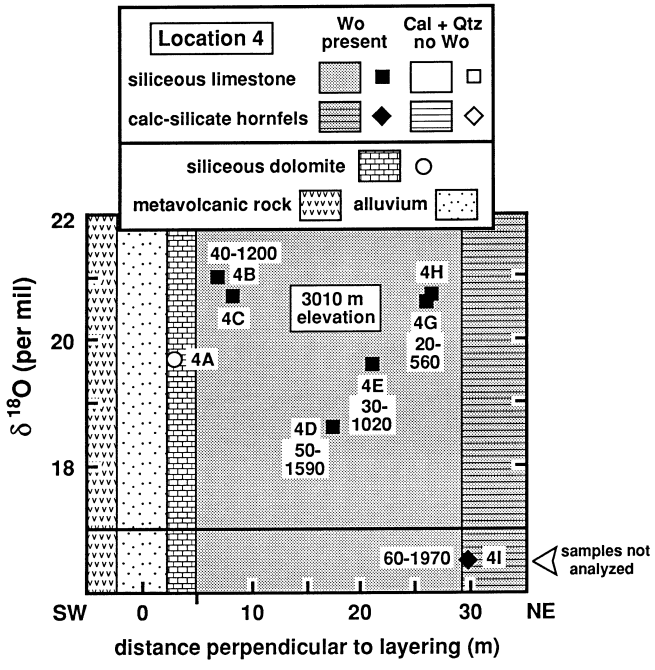

Fig. 6 Lithology and O-isotope composition of the carbonate layer along a traverse perpendicular to strike of lithologic layering at location 4. Other features same as in Figs. 3 and 4

standards indicated that analytical precision for both oxygen and carbon isotope analyses is approximately $\pm 0.1‰$.

All calculations of mineral-fluid equilibria used Berman's (1988) thermodynamic data base updated August, 1990. Fluids were considered CO_2-H_2O solutions that obey the Kerrick and Jacobs (1981) equation of state. The activity of $CaCO_3$ in calcite coexisting with dolomite was calculated from equations in Skippen (1974). Activities of components in silicate minerals were computed using ideal ionic mixing models (Holland and Powell 1990). Molar volumes of minerals were estimated from data in Berman (1988).

Mineralogy and mineral chemistry

Mineralogy

Siliceous limestone and calc-silicate hornfels samples can be divided into two groups, those with wollastonite (Wo) and those without. Both rock types contain calcite (Cal), quartz (Qtz), diopside (Di), plagioclase (Pl), K-feldspar (Kfs), and titanite (Ttn) with various combinations of accessory pyrrhotite (Po), apatite, zircon, tourmaline, scapolite, and pyrite (all mineral abbreviations follow Kretz 1983). Samples with Wo also contain grossular garnet (Grs) but lack tremolite (Tr). All samples with Cal and Qtz but without Wo contain Tr and rarely traces of clinozoisite (Czo) and biotite (Bi) but lack Grs. Thus, the fundamental incompatibility between Wo and Tr described in siliceous carbonate rocks from the Ballachulish aureole (Ferry 1996a) is also seen in the Ritter Range. Mineral assemblages of the siliceous limestone and calc-silicate hornfels samples differ mainly in the relative amounts of Qtz, Cal, Kfs, and Pl.

All siliceous dolomite samples contain Cal, Di, Tr, forsterite (Fo), phlogopite (Phl), and Mg-Al spinel (Spl). Samples from locations 1 and 2 also contain dolomite (Dol). Minor and variable amounts of retrograde serpentine (Srp) and chlorite (Chl) replace Fo and Spl.

Mineral chemistry

Analyzed Cal, Wo, and Grs in siliceous limestone and calc-silicate hornfels samples are close to pure substances (Table 2A, D, K). All plagioclase is anorthite (An), $An_{91–97}$, and Kfs has K/(K + Na) in the narrow range 0.93–0.96 (Table 2I, 2J). Analyzed Di, Tr, and Bi exhibit wider variations in composition. Diopside is a $Ca(Fe,Mg)Si_2O_6$ solution with Fe/(Fe + Mg) = 0.01–0.37. Amphibole and Bi deviate from ideal Tr and Phl principally by minor Fe-Mg, Al_2-MgSi, and F-OH exchange (Table 2G, H). No analyses were obtained of Qtz, Ttn, or accessory minerals.

Analyzed Di, Fo, Phl, Spl, Srp, and Chl in siliceous dolomite samples are close to Mg-rich Fe-Mg solid solutions (Table 2). Spinel exhibits the greatest deviation from a pure Mg compound with Fe/(Fe + Mg) = 0.08–0.09, and Di and Srp show the least deviation with Fe/(Fe + Mg) = 0.02–0.03. Analyzed amphibole in siliceous dolomite samples is pargasite with A-site occupancy by K + Na = 65–87 atom % and 2.3–2.7 Al atoms per formula unit (Table 2G). The measured range in Fe/(Fe + Mg) and F/(F + OH) for amphibole is 0.03–0.04 and 0.08–0.13, respectively. Calcite and Dol are Ca-Mg solutions (Table 2A, B, C). The analyses in Table 2B are of Cal inclusions in Fo that neither show evidence of Dol exsolution nor are in visible communication with matrix Cal via fractures. The Cal inclusions are always richer in Mg than Cal from the matrix of the same sample (e.g., results for sample 2K in Table 2A, B).

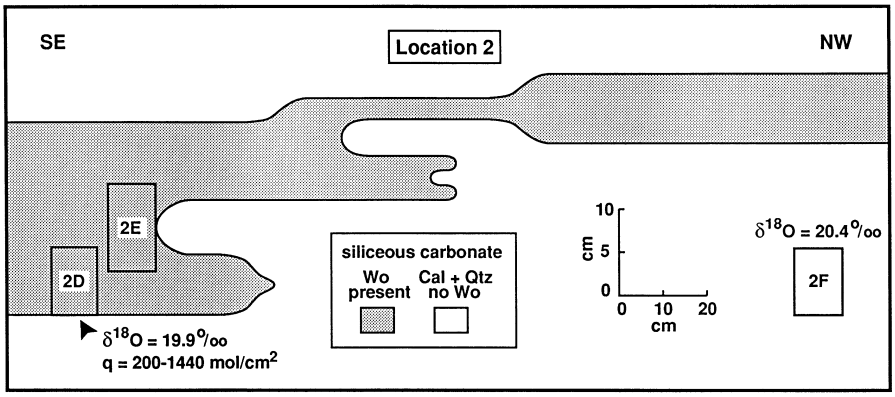

Fig. 7 Distribution of Wo-bearing and Wo-free siliceous limestone in a small area ≈50 m NW of the traverse at location 2. *Rectangles* represent the location and size of samples whose mineralogy was determined from thin sections. There is no significant difference in O-isotope composition between Wo-bearing and Wo-free rocks collected ≈1 m apart along strike of lithologic layering (samples 2D, 2F). The sharp transition from Wo-bearing to Wo-free rocks along individual lithologic layers from SE to NW rules out a significant component of horizontal, layer-parallel metamorphic fluid flow either from SE to NW or vice versa. *Range of numbers* by sample 2D denotes lower and upper bounds on the prograde time-integrated fluid flux associated with formation of Wo and Grs

Each Cal inclusion was analyzed for Si to verify that its higher Mg-content is not an artifact of contamination by host olivine. The composition of Cal inclusions likely reflects conditions of peak metamorphism (cf. Ferry 1996b). Matrix Cal has lower Mg-contents due to retrograde exsolution of Dol.

Mineral reactions

Prograde reactions and the distribution of wollastonite

Prograde mineral-fluid reactions produced Di, Kfs, and An in siliceous limestone and calc-silicate hornfels and Di, Fo, Tr, and Spl in the siliceous dolomite. Because low-grade equivalent rocks are not exposed in the area, the exact nature of these reactions is unknown. Two other prograde mineral reactions can unequivocally be determined. One relates Wo-bearing siliceous limestone and calc-silicate hornfels to their Wo-free counterparts that contain Cal + Qtz.

$$\mathrm{Cal} + \mathrm{Qtz} = \mathrm{Wo} + \mathrm{CO_2}. \quad (1)$$

A second prograde reaction explains the development of Grs, which occurs in all rocks that contain Wo + Cal,

Table 1 Modes of selected samples; volume percent, *tr* < 0.05%. Sample numbers refer to Figs 3–7. (*SD* siliceous dolomite, *SL* siliceous limestone, *CSH* calc-silicate hornfels)

Sample	1D	1H	2D	2H	2K	2N	2O	3B	3L	3O	4A	4D	4G
Rock type	SD	SL	SL	SL	SD	SL	SL	SL	SL	CSH	SD	SL	SL
Calcite	62.90	65.96	32.82	69.68	68.04	73.18	37.86	22.87	37.19	16.09	42.20	24.99	55.75
Dolomite	6.45	0	0	0	7.92	0	0	0	0	0	0	0	0
Wollastonite	0	0	11.19	18.58	0	0	39.62	39.01	0	50.99	0	28.11	tr
Diopside	10.71	5.59	27.60	4.30	4.47	0.05	4.20	5.74	27.91	11.57	32.06	30.75	22.80
Forsterite	10.66	0	0	0	11.65	0	0	0	0	0	10.34	0	0
Amphibole	3.72	1.37	0	0	2.02	3.27	0	0	0.10	0	0.25	0	0
Biotite	3.03	0	0	0	4.72	0	0	0	tr	0	9.54	0	0
Quartz	0	13.34	3.75	1.56	0	16.33	3.32	1.77	10.33	0.89	0	0.05	5.57
Plagioclase	0	6.23	0.89	0.78	0	3.12	0.20	7.11	10.88	7.34	0	5.91	7.32
K-feldspar	0	6.23	9.76	1.22	0	3.36	2.69	13.30	11.58	1.89	0	8.05	6.67
Scapolite	0	0	0	0	0	0	0.05	0	0	0	0	0	0
Garnet	0	0	13.50	3.42	0	0	11.48	8.98	0	9.53	0	1.22	0.60
Spinel	2.13	0	0	0	0.98	0	0	0	0	0	2.88	0	0
Titanite	0	0.44	0.20	0.29	0	0.25	0.39	0.49	0.60	0.45	0	0.24	0.30
Apatite	tr	0.25	0.20	0.05	tr	0	0.10	0.34	0.35	0.40	0.05	0.29	0.20
Zircon	0	0.05	tr	0	0	0	0	tr	0.05	0	0	0	0
Tourmaline	0	0	0	0	0	0.05	0	0	0	0	0	0	0
Pyrite	0	0	0	0	0	0.20	0	0.39	0.55	0	0	0	0
Pyrrhotite	0.35	0.54	0.10	0.10	0.10	0.20	0.10	tr	0	0.84	0.99	0.39	0.80
Clinozoisite	0	0	0	0	0	0	0	0	0.45	0	0	0	0
Chlorite	0.05	0	0	0	0	0	0	0	0	0	0.15	0	0
Serpentine	0	0	0	0	0.10	0	0	0	0	0	1.54	0	0

Table 2 Compositions of minerals in selected samples. Analyses are typically averages of 5 "spot" analyses of 3–5 grains in thin section. *Oxide sum* refers to the sum of metal oxide wt% with all Fe as FeO. Notation for sample numbers and rock types as in footnote to Table 1. All mineral formulas except those for clinozoisite and garnet assume all Fe as Fe^{2+}. Clinozoisite formula assumes all Fe as Fe^{3+}; Fe^{3+}/Fe^{2+} in garnet formulas adjusted to charge balance 12 oxygen atoms

A Matrix calcites[a]

Sample	1D	1H	2D	2H	2K	2N	3B	3L	4A	4D	4G
Rock type	SD	SL	SL	SL	SD	SL	SL	SL	SD	SL	SL
Ca	0.944	0.991	1.000	1.000	0.957	0.993	0.999	0.995	0.960	0.999	0.997
Mg	0.052	0.003	0.000	0.000	0.039	0.005	0.001	0.003	0.036	0.001	0.002
Fe	0.001	0.000	0.000	0.000	0.001	0.000	0.000	0.001	0.002	0.000	0.000
Mn	0.003	0.006	0.000	0.000	0.003	0.002	0.000	0.001	0.002	0.000	0.001
Oxide sum	56.62	55.84	56.36	56.62	56.23	56.52	56.19	56.70	55.73	56.24	56.33

B Calcite inclusions in forsterite[a]

Sample	1C	2I	2K	2M
Rock type	SD	SD	SD	SD
Ca	0.920	0.923	0.925	0.924
Mg	0.065	0.066	0.070	0.068
Fe	0.004	0.003	0.002	0.004
Mn	0.011	0.008	0.003	0.004
Oxide sum	55.77	55.91	55.70	55.35
T (°C)	585°	590°	595°	590°

C Dolomites[b]

Sample	1D	2K
Rock type	SD	SD
Ca	1.019	1.015
Mg	0.962	0.965
Fe	0.013	0.012
Mn	0.006	0.008
Oxide sum	52.07	52.32

D Wollastonites[c]

Sample	2D	2H	3B	4D	4G
Rock type	SL	SL	SL	SL	SL
Ca	0.987	0.984	0.990	0.994	0.994
Fe	0.002	0.007	0.002	0.002	0.001
Mg	0.003	0.002	0.001	0.001	0.001
Mn	0.004	0.002	0.003	0.001	0.001
Si	1.002	1.002	1.001	1.000	1.000
Oxide sum	100.87	100.44	100.80	100.34	100.70

E Diopsides[d]

Sample	1D	1H	2D	2H	2K	2N	3B	3L	4A	4D	4G
Rock type	SD	SL	SL	SL	SD	SL	SL	SL	SD	SL	SL
Ca	0.993	0.994	0.994	1.001	0.984	0.989	1.009	0.997	0.987	0.991	0.995
Na	0.003	0.004	0.004	0.005	0.003	0.004	0.006	0.004	0.003	0.003	0.003
Fe	0.017	0.055	0.177	0.347	0.028	0.014	0.287	0.078	0.021	0.085	0.036
Mg	0.923	0.880	0.782	0.599	0.946	0.947	0.680	0.889	0.916	0.889	0.934
Mn	0.001	0.043	0.018	0.034	0.006	0.005	0.015	0.002	0.001	0.005	0.008
Ti	0.016	0.000	0.001	0.002	0.003	0.001	0.001	0.001	0.011	0.001	0.001
Al^{VI}	0.046	0.012	0.003	0.008	0.024	0.026	0.007	0.018	0.056	0.015	0.016
Al^{IV}	0.068	0.000	0.000	0.001	0.019	0.000	0.014	0.000	0.063	0.000	0.001
Si	1.932	2.004	2.010	1.999	1.981	2.001	1.986	2.002	1.937	2.002	1.999
Oxide sum	100.40	100.31	100.04	100.34	100.90	100.26	100.49	100.51	100.41	100.62	100.71
Fe/(Fe + Mg)	0.018	0.059	0.184	0.367	0.028	0.015	0.297	0.081	0.022	0.088	0.037

F Forsterites[e]

Sample	1D	2K	4A
Rock type	SD	SD	SD
Fe	0.078	0.070	0.085
Mg	1.908	1.928	1.902
Mn	0.009	0.012	0.010
Ca	0.005	0.002	0.003
Si	0.998	0.994	0.998
Oxide sum	100.12	100.24	100.09
Fe/(Fe + Mg)	0.039	0.035	0.043

G Amphiboles[f]

Sample	1D	1H	2K	2N	3L	4A
Rock type	SD	SL	SD	SL	SL	SD
K	0.112	0.012	0.097	0.026	0.002	0.170
Na	0.540	0.000	0.591	0.028	0.020	0.702
Ca	1.973	1.973	1.980	1.995	1.992	1.986
Na	0.028	0.023	0.020	0.005	0.008	0.014
Fe	0.123	0.133	0.127	0.026	0.445	0.167
Mg	4.105	4.709	4.076	4.800	4.411	3.907
Mn	0.011	0.058	0.008	0.005	0.009	0.009
Ti	0.084	0.002	0.091	0.009	0.003	0.181
Al^{VI}	0.723	0.082	0.713	0.127	0.106	0.735
Al^{IV}	1.607	0.038	1.590	0.129	0.072	1.950
Si	6.394	7.962	6.410	7.871	7.928	6.050
F	0.260	0.320	0.172	0.229	0.332	0.173
Oxide sum	98.09	97.89	97.84	98.24	98.29	97.89
Fe/(Fe + Mg)	0.029	0.027	0.030	0.005	0.091	0.041
F/(F + OH)	0.130	0.160	0.086	0.115	0.166	0.086

H Biotites[g]

Sample	1D	2K	3L	4A
Rock type	SD	SD	SL	SD
K	0.836	0.832	0.936	0.859
Na	0.031	0.034	0.005	0.060
Ca	0.010	0.016	0.004	0.003
Fe	0.060	0.057	0.289	0.067
Mg	2.660	2.625	2.497	2.611
Mn	0.002	0.004	0.002	0.001
Ti	0.030	0.037	0.008	0.048
Al^{VI}	0.246	0.256	0.106	0.256
Al^{IV}	1.191	1.187	0.875	1.247
Si	2.809	2.813	3.125	2.753
F	0.072	0.067	1.111	0.088
Oxide sum	95.43	95.32	95.25	95.67
Fe/(Fe + Mg)	0.022	0.021	0.104	0.025
F/(F + OH)	0.036	0.034	0.556	0.044

I Plagioclasesi[h]

Sample	1H	2D	2H	2N	3B	3L	4D	4G
Rock type	SL	SL	SL	SL	SL	SL	SL	SL
X_{an}	0.963	0.924	0.959	0.966	0.933	0.953	0.956	0.969
X_{ab}	0.036	0.066	0.040	0.033	0.064	0.046	0.043	0.030
X_{or}	0.001	0.010	0.001	0.001	0.003	0.001	0.001	0.001
Oxide sum	100.45	100.34	100.39	100.40	100.61	100.49	100.45	100.67

J K-feldspars[h]

Sample	1H	2D	2H	2N	3B	3L	4D	4G
Rock type	SL	SL	SL	SL	SL	SL	SL	SL
X_{or}	0.955	0.956	0.938	0.953	0.928	0.954	0.933	0.951
X_{ab}	0.041	0.035	0.040	0.038	0.067	0.043	0.060	0.045
X_{an}	0.004	0.009	0.007	0.009	0.005	0.003	0.007	0.004
X_{cs}	0.000	0.000	0.015	0.000	0.000	0.000	0.000	0.000
Oxide sum	100.25	99.65	99.64	100.48	99.52	100.68	99.93	99.85

K Garnets[i]

Sample	2D	2H	3B	4D	4G
Rock type	SL	SL	SL	SL	SL
Ca	2.955	2.957	2.979	2.992	2.967
Fe^{2+}	0.002	0.000	0.013	0.039	0.015
Mg	0.028	0.007	0.007	0.005	0.006

Table 2 (continued)
K Garnets[i]

Sample	2D	2H	3B	4D	4G
Rock type	SL	SL	SL	SL	SL
Mn	0.013	0.032	0.014	0.011	0.021
Al	1.961	1.973	2.003	1.970	2.005
Fe^{3+}	0.044	0.049	0.000	0.000	0.000
Ti	0.016	0.004	0.006	0.009	0.008
Si	2.981	2.979	2.986	2.991	2.981
Oxide sum	100.03	100.12	100.08	100.71	100.10

L Spinels[e]

Sample	1D	2K	4A
Rock type	SD	SD	SD
Fe	0.081	0.081	0.086
Mg	0.899	0.899	0.896
Mn	0.004	0.007	0.005
Ca	0.003	0.006	0.004
Ti	0.001	0.001	0.001
Al	2.003	2.004	2.000
Oxide sum	100.17	100.29	99.55
Fe/(Fe + Mg)	0.083	0.083	0.087

M Clinozoisite[j]

Sample	3L
Rock type	SL
Ca	1.977
Mg	0.004
Mn	0.000
Al	2.943
Fe^{3+}	0.057
Ti	0.000
Si	3.009
Oxide sum	98.25
Al/(Al + Fe)	0.981

N Chlorites[k]

Sample	1D	4A
Rock type	SD	SD
Fe	0.107	0.223
Mg	4.604	4.830
Mn	0.000	0.032
Ti	0.000	0.003
Al	2.272	1.499
Si	2.933	3.320
Oxide sum	86.74	86.72
Fe/(Fe + Mg)	0.023	0.044

O Serpentine[k]

Sample	4A
Rock type	SD
Fe	0.137
Mg	5.350
Mn	0.006
Ti	0.000
Al	0.690
Si	3.728
Oxide Sum	86.55
Fe/(Fe + Mg)	0.025

[a] Calcites: cations per oxygen atom (less CO_2). Calcite inclusions in forsterite are the most magnesian analyzed in the sample. Temperature (Table 2B) estimated from the composition of Cal in equilibrium with Dol (Anovitz and Essene 1987)
[b] Dolomites: cations per 2 oxygen atoms (less CO_2)
[c] Wollastonites: cations per 3 oxygen atoms
[d] Diopsides: cations per 6 oxygen atoms
[e] Forsterites and spinels: cations per 4 oxygen atoms
[f] Amphiboles: cations per 23 oxygen atoms (less H_2O)
[g] Biotites: cations per 11 oxygen atoms (less H_2O)
[h] Feldspars: mole fraction anorthite (*an*), albite (*ab*), orthoclase (*or*), and celsian (*cs*) components. When Ba was detected by EDS; Ba atoms pfu and wt% BaO were estimated from measured Al-content and stoichiometry
[i] Garnets: cations per 8 cations
[j] Clinozoisite: cations per 12.5 oxygen atoms (less H_2O)
[k] Chlorites and serpentine: cations per 14 oxygen atoms (less H_2O)

typically as a reaction rim around An grains. Garnet is not observed in samples either with An + Cal ± Qtz without Wo, or with An + Wo without Cal. The likely reaction therefore is:

$$An + Wo + Cal = Grs + CO_2. \quad (2)$$

Although Reaction 2 for practical purposes went to completion in most Wo-bearing rocks with the consumption of An (Table 1), some samples contain An grains rimmed by Grs, which isolated the plagioclase from further reaction with Wo and Cal (Fig. 8A).

The spatial distribution of Wo in contact aureoles records the geometry and amount of fluid flow during metamorphism (Ferry 1991). Distinctive differences in color and texture between Wo-bearing and Wo-free rocks allowed us to map the distribution of Wo in the field (Figs. 3–7). The mapping criteria were verified by examination of thin sections of 36 samples of limestone and hornfels collected from locations 1–4. Wollastonite occurs in the carbonate layer close to the exposure of granodiorite at Thousand Island Lake and is absent from the unit more than ≈600 m from the lake. The southeasternmost occurrence of Wo in the carbonate layer is marked on Fig. 2. Southeast of the limit, as at location 1, Cal + Qtz is ubiquitous in limestone and hornfels across the entire carbonate layer and Wo is absent (Fig. 3). Close to the exposure of granodiorite, as at location 4, Wo occurs in all samples of limestone and

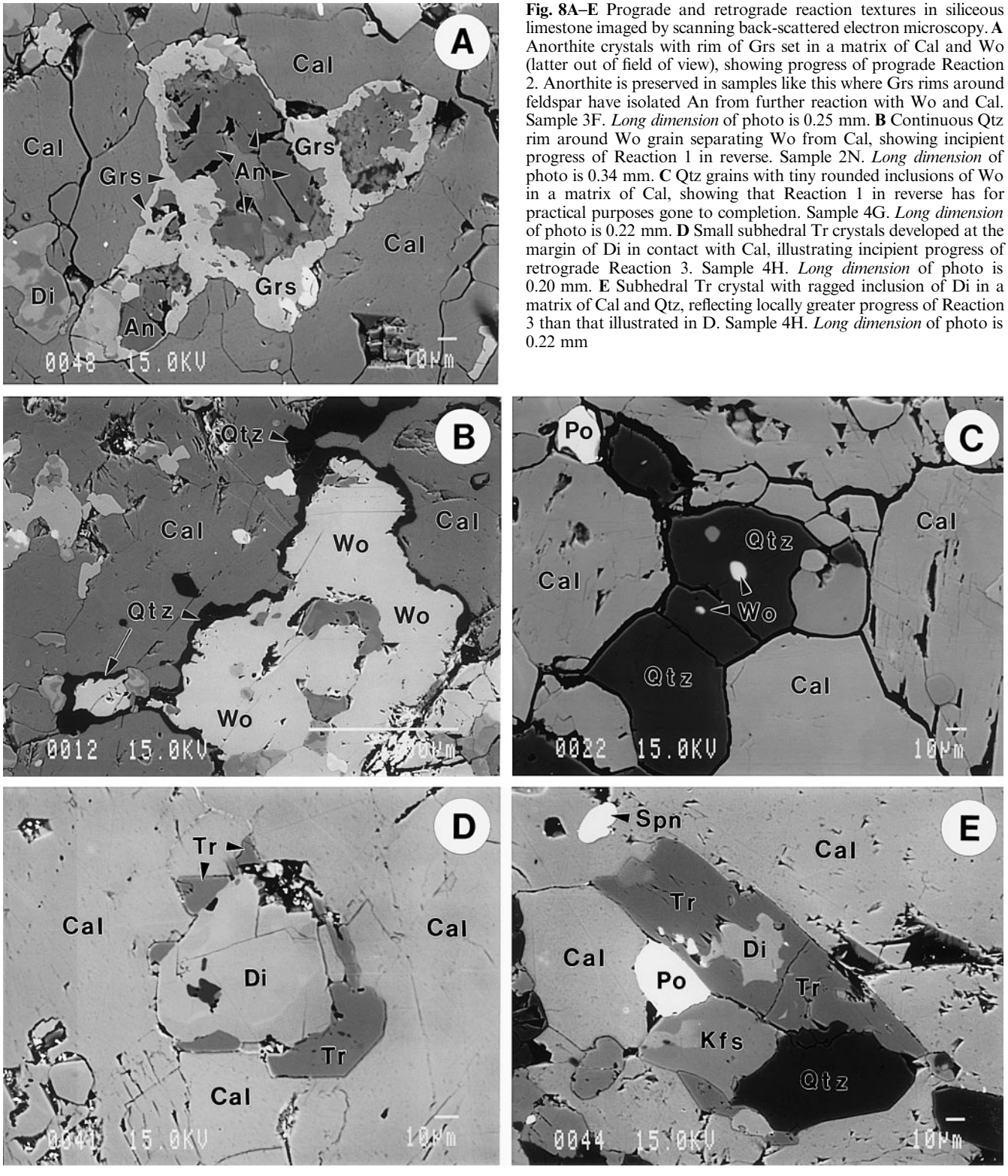

Fig. 8A–E Prograde and retrograde reaction textures in siliceous limestone imaged by scanning back-scattered electron microscopy. **A** Anorthite crystals with rim of Grs set in a matrix of Cal and Wo (latter out of field of view), showing progress of prograde Reaction 2. Anorthite is preserved in samples like this where Grs rims around feldspar have isolated An from further reaction with Wo and Cal. Sample 3F. *Long dimension* of photo is 0.25 mm. **B** Continuous Qtz rim around Wo grain separating Wo from Cal, showing incipient progress of Reaction 1 in reverse. Sample 2N. *Long dimension* of photo is 0.34 mm. **C** Qtz grains with tiny rounded inclusions of Wo in a matrix of Cal, showing that Reaction 1 in reverse has for practical purposes gone to completion. Sample 4G. *Long dimension* of photo is 0.22 mm. **D** Small subhedral Tr crystals developed at the margin of Di in contact with Cal, illustrating incipient progress of retrograde Reaction 3. Sample 4H. *Long dimension* of photo is 0.20 mm. **E** Subhedral Tr crystal with ragged inclusion of Di in a matrix of Cal and Qtz, reflecting locally greater progress of Reaction 3 than that illustrated in D. Sample 4H. *Long dimension* of photo is 0.22 mm

hornfels (Fig. 6). Because of the difference in elevation between locations 1 and 4, the distribution of Wo in map view also corresponds to its vertical distribution. Wollastonite occurs at relatively low elevations in the study area. Its limit in the vertical direction corresponds to the elevation of the carbonate layer where Wo disappears to the southeast (3090 m). At the scale of Fig. 2 Wo-bearing rocks are exposed over a horizontal distance of ≈ 1.2 km and a vertical distance of ≈ 90 m. The spatial association of Wo with exposures of granodiorite

suggests that reaction 1 took place during prograde contact metamorphism caused by emplacement of the pluton.

Rocks both with and without Wo occur in the carbonate layer between the southeastern limit of Wo and location 3. The distribution of Wo versus Cal + Qtz in limestone and hornfels was mapped at the dm scale at locations 2 and 3 (Figs. 4, 5). At location 2, Wo-bearing rocks only occur in two zones, each $\approx$1 m wide, at contacts between: (1) the upper limestone and metavolcanic rock; (2) the lower limestone and calc-silicate hornfels. Wollastonite is absent from the calc-silicate hornfels. The distribution of Wo is similar between location 2 and the southeastern limit of Wo. Wollastonite is ubiquitous in the calc-silicate hornfels at location 3 and occurs in siliceous limestone at all its contacts with metavolcanic rock or calc-silicate hornfels (Fig. 5). Both the upper and lower limestones, however, contain a core of Wo-free rocks, 2–7 m wide. Wollastonite is preferentially developed at locations 2 and 3 on the dm scale along contacts between limestone and either metavolcanic rock or hornfels.

Rocks that contain Wo alternate with rocks that contain Cal + Qtz in zones parallel to layering on a cm to dm scale near location 2 (Fig. 7). Wollastonite-bearing rock passes into Wo-free rock with Cal + Qtz along individual lithologic layers both from SE to NW and vice versa. Interfingering of Wo-bearing and Wo-free rocks is common between locations 2 and 3.

Retrograde reactions

Textures of the siliceous limestone show evidence for significant retrograde mineral-fluid reaction (Fig. 8). All limestones have bulk compositions such that Reaction 1 goes to completion with the consumption of Qtz. Nevertheless, every Wo-bearing rock contains trace amounts to several modal% Qtz (Table 1). In samples with <1 modal% Qtz, Qtz exclusively occurs as thin rims that separate Wo grains from Cal (Fig. 8B). In rocks with several modal% Qtz, Qtz occurs as equant grains that commonly contain rounded, μ-sized inclusions of Wo (Fig. 8C). Textures illustrated in Fig. 8B and C imply that Reaction 1 progressed in reverse during retrograde metamorphism as the aureole cooled, producing Qtz in Wo-bearing limestone and hornfels that were Qtz-free at peak metamorphic conditions.

All Wo-free siliceous limestone and calc-silicate hornfels samples contain Tr that typically exhibits a close spatial and textural relationship with Di. In parts of samples where Tr shows incipient development, it occurs as subhedral crystals that radiate from Di grains (Fig. 8D). Where Tr is extensively developed, it occurs as subhedral crystals that contain ragged Di inclusions which are associated with Cal and Qtz (Fig. 8E). Textures illustrated in Fig. 8D and E imply the reaction:

$$5\ \mathrm{Di} + 3\ \mathrm{CO_2} + \mathrm{H_2O} = \mathrm{Tr} + 3\ \mathrm{Cal} + 2\ \mathrm{Qtz}. \quad (3)$$

Because Tr is stable in limestone and hornfels at T at least 65 °C below the peak value (see below), Reaction 3 must have occurred during retrograde metamorphism; the siliceous limestone and calc-silicate hornfels were Di-bearing and Tr-free at the thermal maximum.

Retrograde mineral-fluid reactions also produced Srp from Fo and Chl from Spl in some siliceous dolomite samples. Because this study focused on siliceous limestone and calc-silicate hornfels, the Srp- and Chl-forming reactions are not considered further. In other aureoles, contact metamorphosed Fo-bearing siliceous dolomites commonly contain retrograde Tr (e.g., Ferry 1996a, b; Ferry and Rumble 1997). Retrograde Tr can be distinguished from prograde Tr both by texture and by the lower Na-, K-, Al-, and F-contents of retrograde compared to prograde amphibole (Ferry 1996a, b). No Tr of unequivocal retrograde origin was identified in siliceous dolomite from the Ritter Range.

Stable isotope geochemistry

Measured isotopic compositions

The measured oxygen and carbon isotope compositions of Cal in 28 samples of siliceous dolomite, siliceous limestone, and calc-silicate hornfels are listed in Table 3 and illustrated in Fig. 9A. The spatial distributions of O-isotope compositions at locations 1–4 appear in Figs. 3–7. Values of $\delta^{18}O$ and $\delta^{13}C$ are in the range 17.1 to 21.0‰ and −6.2 to +1.0‰, respectively, for limestone and hornfels samples. The range of $\delta^{18}O$ and $\delta^{13}C$ values for siliceous dolomite samples is narrower, 19.7 to 21.5‰ and −2.3 to −0.4‰, respectively. There are no systematic differences in O- and C-isotope compositions between Wo-bearing and Wo-free limestone and hornfels samples (Fig. 9A). No systematic spatial patterns of O-isotope compositions appear on the scale of 1–100 m (Figs. 3–7). Samples of ^{18}O-depleted, Wo-bearing calc-silicate rock, like specimen B86-87b ($\delta^{18}O$ = 14.1‰) collected by Hanson et al. (1993) near Garnet Lake, were not observed.

Isotopic compositions corrected for devolatilization reaction

To evaluate whether the isotopic compositions of these rocks were in part controlled by interaction with an isotopically exotic fluid, the effect of metamorphic devolatilization reactions was removed, using the standard equation for Rayleigh distillation (Valley 1986), from values for 18 samples for which there are modal and O- and C-isotope data. Calculations assumed that one mole of CO_2 was liberated for every mole of Ca, Mg, and Fe now in silicate minerals (from modal and mineral composition data); the assumption is equivalent to consider-

Table 3 Isotopic composition of calcite in selected samples. Values of $\delta^{18}O$ and $\delta^{13}C$ in per mil relative to VSMOW and VPDB, respectively. Measured values determined by direct analysis; values corrected for devolitilization reaction computed from Rayleigh fractionation model described in text (*NC* not computed). Notation for sample numbers and rock types as in footnote to Table 1. Distance is measured perpendicular to bedding from 0 at the SW margin of the carbonate band (*NM* not measured). *Wo* identifies whether Wo is present in (*P*) or absent (*A*) from sample

Sample	Distance (m)	Rock type	Wo	$\delta^{18}O$ Measured	$\delta^{13}C$ Measured	$\delta^{18}O$ Corrected for reaction	$\delta^{13}C$ Corrected for reaction
1C	5.3	SD	A	20.7	−1.4	NC	NC
1D	12.3	SD	A	21.0	−0.4	22.0	0.6
1E	16.5	SL	A	20.9	−1.7	NC	NC
1G	31.1	SL	A	19.9	0.1	NC	NC
1H	36.0	SL	A	19.9	−0.6	20.3	−0.2
1I	40.5	CSH	A	18.9	−5.1	20.2	0.2
2D	NM	SL	P	19.9	−2.7	21.7	0.2
2F	NM	SL	A	20.4	0.2	NC	NC
2G	0.1	SL	P	19.0	−1.0	NC	NC
2H	0.3	SL	P	18.4	−3.3	19.3	−2.4
2I	1.1	SD	A	21.5	−0.9	NC	NC
2K	4.7	SD	A	21.0	−0.8	21.9	0.1
2M	12.0	SD	A	21.5	−1.0	NC	NC
2N	15.3	SL	A	19.3	1.0	19.4	1.2
2O	16.5	SL	P	19.1	−6.0	20.9	−3.4
3B	0.2	SL	P	18.5	−5.2	20.3	−1.6
3F	3.7	SL	P	18.4	−1.6	19.3	−0.6
3G	5.5	SL	A	18.1	−1.7	NC	NC
3L	23.9	SL	A	18.6	−4.7	19.9	−2.6
3N	29.5	CSH	P	19.3	−2.6	21.0	0.2
3O	30.5	CSH	P	17.1	−6.2	19.5	−1.0
4A	2.9	SD	A	19.7	−2.3	21.3	0.1
4B	6.9	SL	P	21.0	0.2	22.0	1.2
4C	8.2	SL	P	20.7	0.0	NC	NC
4D	17.4	SL	P	18.6	−4.5	20.7	−0.7
4E	21.1	SL	P	19.6	−2.4	20.5	−1.4
4G	26.0	SL	P	20.6	−1.6	21.7	−0.3
4H	26.3	SL	P	20.7	−2.0	NC	NC

ing that all Ca, Mg, and Fe in siliceous carbonate rock prior to metamorphism was sited in calcite and dolomite or ankerite (e.g., Ferry 1994). Oxygen and C were assumed to have been lost only as CO_2, and the fraction of O and C remaining in the rock was computed using measured amounts in each sample (from modal and mineral composition data) and the inferred loss of CO_2. Values of α_{CO_2}-rock for O and C isotopes, 1.006 and 1.003, respectively, were adopted from Valley (1986) and Nabelek (1991).

If the effect of devolatilization reaction is removed, the isotopic compositions of all rock types shift to higher values and fall in a narrower range compared to measured values (Table 3, Fig. 9B). Corrected compositions for limestone and hornfels samples are in the ranges $\delta^{18}O = 19.3$ to 22.0‰ and $\delta^{13}C = -3.4$ to $+1.2$‰, res-

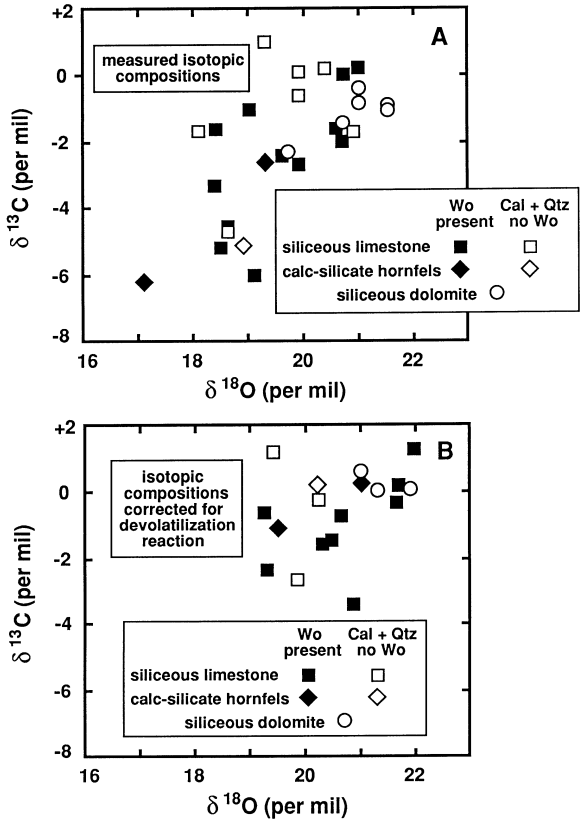

Fig. 9A, B Oxygen- and C-isotope compositions of siliceous limestone, calc-silicate hornfels, and siliceous dolomite. **A** Measured compositions. **B** Isotopic compositions corrected for the effect of prograde devolatilization reactions using Rayleigh distillation model described in text. The overlap in composition between Wo-bearing and Wo-free rocks and the significant difference in isotopic composition between the siliceous carbonate rocks and both the granodiorite and metavolcanic rocks from the study area indicate that none of the analyzed Wo-bearing rocks exposed in the study area have isotopic compositions altered by metamorphic fluid flow. Any isotope alteration front must lie upstream from the present level of exposure

pectively; the corresponding ranges for siliceous dolomite are $\delta^{18}O = 21.3$ to $22.0^{o}/_{oo}$ and $\delta^{13}C = 0.1$ to $0.6^{o}/_{oo}$. The range of corrected isotopic compositions for Wo-bearing samples overlaps with that of Wo-free ones (Fig. 9B).

Pressure, temperature, and fluid composition

Pressure and temperature

Peak T was calculated from the composition of Cal inclusions in Fo from siliceous dolomite samples from locations 1 and 2 (Fig. 10). Because the samples contain Dol, the Cal inclusions coexisted with Dol when they formed. Values of T calculated from the composition of Cal inclusions are minimum estimates of peak conditions if the inclusions were trapped prior to the thermal maximum. In other contact aureoles, however, Cal inclusions in Fo appear to record the peak T as independently determined from mineral equilibria in other rock types (e.g., Ferry 1996b). Using the calibration of Anovitz and Essene (1987), Cal inclusions in Fo record $T = 585$ °C at location 1 and $T = 590$–595 °C at location 2 (Table 2B).

The coexistence of andalusite (And) and Kfs (Fig. 1) places an upper bound on peak P of 2200 bars (assuming unit activity of H_2O and equilibrium Al-Si ordering in Kfs). If the Cal, Dol, Tr, Fo, and Di in siliceous dolomite samples at locations 1 and 2 were in equilibrium with a CO_2-H_2O fluid, the occurrence of And and the absence of sillimanite (Sil) in the area limits P to <2000 bars regardless of T. The most precise estimate of peak P is based on the univariant equilibrium among Tr, Dol, Cal, Fo, Di, and CO_2-H_2O fluid at peak $T = 585$–595 °C, 1400–1600 bars (Fig. 10).

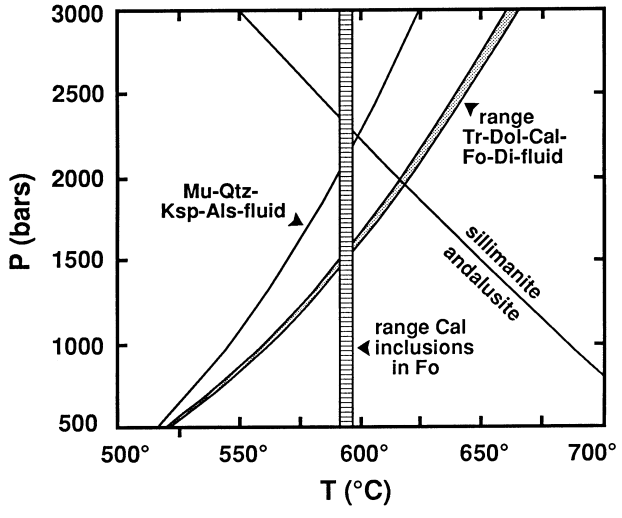

Fig. 10 Constraints on metamorphic P and T imposed by mineral equilibria. *Curves* for And-Sil and muscovite (Mu)-Qtz-Ksp-aluminum silicate (Als)-H_2O fluid equilibria assume all phases are pure substances. *Band* for Tr-Dol-Cal-Fo-Di-fluid equilibrium corresponds to the range of P and T consistent with the variation in measured mineral compositions in all analyzed samples. The Tr-Dol-Cal-Fo-Di-fluid equilibrium represents the trace of isobaric invariant points from T-X_{CO_2} diagrams at 500–3000 bars in P-T space; fluid composition therefore varies continuously with P and T for the equilibrium. Vertical band represents range in maximum T recorded by Cal inclusions in Fo from 4 samples of siliceous dolomite (see text and Table 2B). The preferred estimate of peak P and T, 1500 bars and 595 °C, assumes that P is recorded by the Tr-Dol-Cal-Fo-Di-fluid equilibrium at the maximum calculated Cal-Dol T

Because T calculated from Cal-Dol thermometry represents a minimum, the preferred estimate of peak T in the study area was considered the maximum recorded value, 595 °C. The preferred estimate of peak P is 1500 bars. These values are consistent with the presence of And + Kfs in a nearby meta-ashflow tuff unit (Fig. 1) and the absence of Sil from the study area. Because the carbonate layer is almost parallel to the And + Kfs isograd (Figs. 1, 2) and because of the small area of Fig. 2, values of P and T at the peak of contact metamorphism probably varied only slightly in the carbonate layer in the study area. The error in Cal-Dol thermometry introduced by an error of ±1 mol% $MgCO_3$ component in Cal (the maximum likely from microprobe analysis) is ±20–25 °C. The uncertainty in peak T therefore was considered ±25 °C. The absence of Sil from the study area indicates that the estimated peak P is unlikely to be more than 500 bars too low. At peak $T = 595$ °C, the stable coexistence of Dol + Di in siliceous dolomite at locations 1 and 2 sets a lower limit on p_{CO_2}, and hence on P_{total}, of 1440 bars. As a conservative measure, however, the uncertainty in the lower bound on peak P was taken as the same as the uncertainty in the upper bound, 500 bars.

The T of retrograde Reaction 3 is also constrained if it proceeded at or near equilibrium. Amphibole could not have developed at T above the maximum for equilibrium among Tr, Cal, Qtz, Di, and CO_2-H_2O fluid. Using estimated activities of components in mineral solutions based on measured compositions of coexisting Tr, Di, and Cal, the T maximum is 515–530 °C at 1500 bars. Retrograde amphibole thus developed at 65 °C or more below the inferred peak T.

Fluid composition during prograde metamorphism

The lower bound on X_{CO_2} of prograde fluid in equilibrium with siliceous limestone and calc-silicate hornfels near peak conditions is set by the formation of Grs by Reaction 2 ($X_{CO_2} = 0.13$); the upper bound on $X_{CO_2} = 0.28$ is set by formation of Wo by reaction 1 at the inferred peak P-T conditions (Fig. 11). Uncertainties in peak P expand these limits to 0.12 to 0.52; uncertainties in peak T yield limits of 0.13 to 0.44. The composition of peak metamorphic fluid in equilibrium with siliceous dolomite was almost pure CO_2. At 1500 bars the isobaric invariant equilibrium among Tr, Dol, Cal, Fo, Di, and fluid in 4 analyzed samples from locations 1 and 2 records $X_{CO_2} = 0.96$ to 0.98. At 1500 bars and 595 °C, the univariant equilibrium among Tr,

Cal, Fo, and Di, that corresponds to the observed mineral assemblage in sample 4A, records $X_{CO_2} > 0.99$. Evidently mineral-fluid equilibria at the peak of metamorphism buffered fluid composition, producing fluid with significantly different X_{CO_2} values in lithologic layers only a few m apart.

The T-X_{CO_2} paths of retrograde metamorphism

Reaction 1 in reverse buffered fluid composition in Wo-bearing rocks during retrograde metamorphism along the Wo-Cal-Qtz equilibrium with decreasing T, provided equilibrium was attained or closely approached (solid shaded curve in Fig. 11). If the reverse of Reaction 1 began as soon as the aureole started to cool, the retrograde T-X_{CO_2} path in Wo-bearing rocks was initiated at 595 °C and $X_{CO_2} = 0.28$; if Reaction 1 began at lower T, the path was initiated at lower X_{CO_2}. Although the precise value of T and X_{CO_2} at which Tr first developed in Wo-free limestone and hornfels cannot be determined, Reaction 3 buffered fluid composition along the corresponding univariant curve (dashed, shaded curve in Fig. 11). The T-X_{CO_2} paths of retrograde metamorphism in Fig. 11 explain the mutual incompatibility between Wo and Tr in limestone and hornfels. As T decreased, Reaction 1 buffered X_{CO_2} to values too low for Reaction 3 to occur in Wo-bearing rocks. In the absence of Wo, however, more CO_2-rich fluids were possible and Di was altered to Tr by Reaction 3. An unresolved problem with the proposed T-X_{CO_2} path of retrograde metamorphism for Wo-bearing rocks is the absence of textural evidence for conversion of Grs to An + Wo + Cal by the reverse of Reaction 2. The lack of reaction may result from the refractory character of garnet.

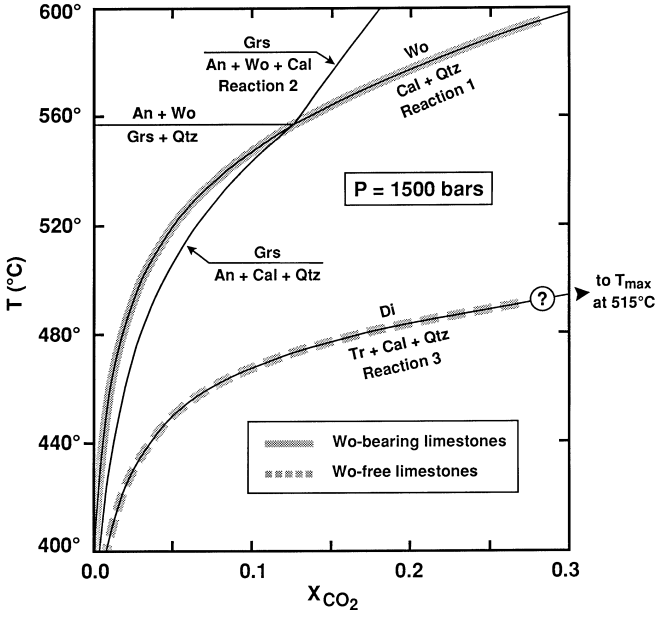

Fig. 11 T-X_{CO_2} diagram illustrating selected phase equilibria among Cal, Qtz, Wo, Grs, An, Di, Tr, and CO_2-H_2O fluid at 1500 bars. All minerals considered pure substances. *Shaded solid* and *shaded dashed curves* illustrate the T-X_{CO_2} evolution of Wo-bearing and Wo-free siliceous limestone, respectively, during retrograde mineral-fluid reaction. *Question mark* denotes uncertainty in T and X_{CO_2} at which Reaction 3 initiated

Fluid flow during contact metamorphism

Mineralogical evidence for fluid infiltration of siliceous carbonate rocks

Wollastonite developed by a decarbonation reaction while rocks were in equilibrium with CO_2-H_2O fluid with X_{CO_2} significantly <1. This is evidence that Reaction 1 was driven by infiltration of rocks by chemically reactive, relatively H_2O-rich fluids (Ferry 1991). Retrograde development of Qtz by the reverse of Reaction 1 and of Tr by Reaction 3 was caused by carbonation/hydration reactions. The retrograde reactions therefore record infiltration of the carbonate rocks by CO_2-H_2O fluids as the aureole cooled.

Prograde fluid flow

Geometry of flow and source of the infiltrating fluid

When chemically reactive H_2O-rich fluid flows through rocks that contain Cal + Qtz and mineral-fluid equilibrium is attained or approached, flow drives formation of Wo by Reaction 1 (Ferry 1991). The mapped distribution of Wo-bearing rocks produced by Reaction 1 images where chemically reactive fluids infiltrated the siliceous carbonate layer during contact metamorphism (Figs. 2–7) which, in turn, constrains the geometry of flow. Four end-member flow geometries are: (1) across layering; (2) horizontal, parallel to layering from SE to NW; (3) horizontal, parallel to layering from NW to SE; (4) parallel to layering along dip. Because alternation of Wo-bearing and Wo-free rocks along a flow path is impossible, the layer-by-layer alternation of Wo-bearing and Wo-free siliceous limestone at locations 2 and 3 rules out metamorphic fluid flow with a significant component across layering at the present level of exposure. As in many other contact and regional metamorphic terranes worldwide, flow evidently was largely or entirely parallel to lithologic layering (cf. Bowman et al. 1994; Ferry 1994; Kohn and Valley 1994; Skelton 1996).

If flow was horizontal and layer-parallel from SE to NW in the area of Fig. 2, it should have been toward the exposure of granodiorite at Thousand Island Lake, in the direction of increasing T. When infiltration drives Reaction 1 under these circumstances, transport theory predicts that: (1) Wo-free rocks with Cal + Qtz should pass along the flow path in any particular layer from SE to NW into Wo-bearing rocks; (2) reactants and products will occur together in individual samples for a sig-

nificant distance interval along the flow path, unless time-integrated flux is large (Ferry 1991). Neither prediction is met in the study area. Between locations 2 and 3 layers of Wo-bearing limestone pass from SE to NW into Wo-free rocks with Cal + Qtz (Fig. 7). Although Cal and Qtz are ubiquitous in Wo-bearing rocks, their textures indicate that the Qtz is retrograde (Fig. 8B, C), and Wo-bearing rocks were Qtz-free at the peak of metamorphism. Horizontal, SE-to-NW, layer-parallel flow is ruled out.

If flow was horizontal and layer-parallel from NW to SE in the area of Fig. 2, it would have been in the direction of decreasing T. Infiltration under these circumstances could drive Reaction 1 if the input fluid were relatively H_2O-rich and out of equilibrium with Cal + Qtz. Transport theory predicts that Wo-bearing rocks upstream should pass along the flow path in any particular layer from NW to SE into Wo-free rocks with Cal + Qtz downstream (Ferry 1991). Between locations 2 and 3, however, numerous layers of Wo-free limestone with Cal + Qtz pass from NW to SE into Wo-bearing rocks (e.g., Fig. 7). Horizontal, NW-to-SE layer-parallel flow is not likely.

The one geometry of metamorphic fluid flow most consistent with observed distributions of Wo-bearing and Wo-free rocks at all scales is layer-parallel along dip. Because the mechanics of downward flow of fluid in rocks at lithostatic P is problematic (Walther and Orville 1982; Hanson 1992; Hanson et al. 1993), flow must have been up-dip rather than down-dip. Upward layer-parallel flow would have been in the direction of decreasing T, and Reaction 1 driven by input of relatively H_2O-rich fluid out of equilibrium with Cal + Qtz. In this case, Wo would have developed along an upward-moving reaction front separating Wo-bearing rock below from Wo-free rock with Cal + Qtz above (Ferry 1991). The source of aqueous fluid could have been the crystallizing granodiorite, metamorphic dehydration reactions at depth in metavolcanic rocks, or a combination of the two. If the granodiorite was the source, the carbonate layer is likely cut by the pluton at depth. If the metavolcanic rocks were the source, some component of cross-layer fluid flow must have occurred below the present level of exposure. Figure 12 illustrates, in cross section and approximately to scale, the inferred geometry of the Wo-reaction front viewed perpendicular to strike of the siliceous carbonate layer. The fingering at the leading edge of the reaction front, shown schematically on Fig. 12 in the elevation range 3060–3090 m, is based on exposures like those illustrated in Figs. 4, 5, and 7. The actual scale of fingering in these exposures varies from cms to several tens of m in both the vertical and horizontal dimensions. The development of such fingers is consistent with numerical simulations of coupled fluid flow and chemical reaction in porous media in which permeability parallel to the direction of flow is greater than perpendicular to it (Lichtner 1996).

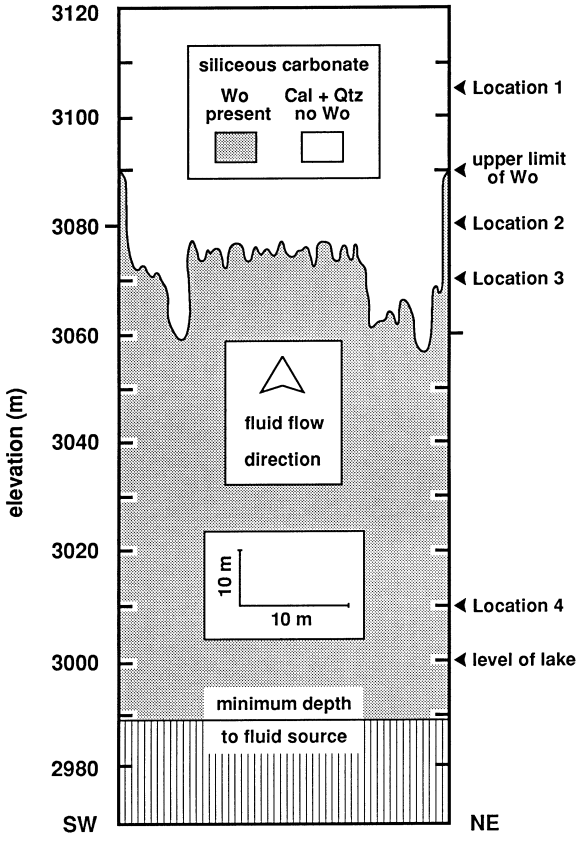

Fig. 12 Cross section through the siliceous carbonate layer, approximately to scale, illustrating the geometry of the upwardly transported Wo-reaction front within siliceous limestone. For simplicity, siliceous dolomite at locations 1, 2, and 4 and the internal metavolcanic layer at location 3 are omitted; the aggregate of limestone and dolomite everywhere considered 30 m thick; and the dip of lithologic layering is taken as vertical. Distribution of Wo-bearing and Wo-free rocks at the elevations of locations 1–4 are taken from Figs. 3–6. Fine structure of the reaction front copied from figures in Lichtner (1996). Minimum depth to fluid source explained in text

Estimates of the amount of prograde fluid flow

A lower limit on the amount of fluid that infiltrated the carbonate layer as Reaction 1 took place was estimated from the upward limit of the mineral reaction front and from the measured O-isotope compositions of rocks from location 4. Measured values of whole-rock $\delta^{18}O$ for granodiorite and nearby metavolcanic rocks (Fig. 1) are 9.0‰ and 7.4 to 13.6‰, respectively (Hanson et al. 1993). The analyzed Cal in Wo-free limestone has much higher $\delta^{18}O$ values of 18.1 to 20.9‰ (Table 3). Regardless whether the source of fluid was the granodiorite or the metavolcanic rocks (or both), infiltration of aqueous fluid into carbonate rock would drive an O-isotope alteration front. The distance (z) between the front and the inlet to the flow system is related to molar time-integrated flux (q°) at the inlet by:

$$z = q^\circ (N_f / V_r) \tag{4}$$

where N_f is the moles O per mole fluid and V_r is the moles O per unit volume of rock (Dipple and Ferry 1992). A reaction front that formed Grs by Reaction 2 coincided with the one that formed Wo by Reaction 1 during infiltration-driven metamorphism in the Ritter Range pendant. The distance (z) that the two reaction fronts travelled from the inlet of the flow system is related to molar time-integrated flux (q) at the present level of exposure by:

$$q = (\xi_{\max}) \int_0^z \left(\frac{1 - X_{CO_2}}{X_{CO_2} - X^{\circ}_{CO_2}} \right) dz + \xi_{\max} z \qquad (5)$$

where $\xi_{\max}$ is the sum of the values of reaction progress at which Reactions 1 and 2 go to completion, $\xi_{\max} z$ is the internal production of CO_2 along the flow path by reaction between 0 and z ($q = q^{\circ} + \xi_{\max} z$), X_{CO_2} is the composition of fluid at the leading edge of the reaction front, and $X^{\circ}_{CO_2}$ is the composition of fluid introduced at the inlet of the flow system (Ferry 1996a). Both Eqs. 4 and 5 assume negligible mass transport by diffusion and dispersion and local mineral-fluid equilibrium at all points along the flow path. If the input fluid was H_2O (as would be appropriate for fluid derived either from the granodiorite or dehydration reactions in the metavolcanic rocks), $N_f = 1$ and $X^{\circ}_{CO_2} = 0$. The value adopted for V_r was 0.0816 mol/cm^3, the O-content of a rock with equal proportions of Cal, Qtz, and Wo on a mole basis (V_r is relatively insensitive to mineralogy). The value taken for $\xi_{\max}$ was $7.4 \cdot 10^{-3}$ mol/cm^3, the sum of the average inferred Wo-content of all analyzed rocks after the completion of Reaction 1 ($7.0 \cdot 10^{-3}$ mol/cm^3, the average of the sum of measured Wo, Qtz, and Grs contents) and the rocks' average inferred Grs content after completion of Reaction 2 ($0.4 \cdot 10^{-3}$ mol/cm^3, the average of measured Grs contents). For individual samples $\xi_{\max}$ varies in the range $2.6–14.7 \cdot 10^{-3}$ mol/cm^3. Because Reaction 2 on average makes only a minor ($\approx 5\%$) contribution to the total amount of decarbonation, the mineral reaction front is referred to as the Wo-reaction front. Application of Eq. 4 for practical purposes is independent of variations in P and T along the flow path. Equation 5 was applied assuming mineral-fluid reaction at peak P-T conditions at the level of exposure of location 2. The P gradient along the flow path, dP/dz, was considered −270 bars/km, appropriate for upward near-vertical flow of fluid at lithostatic P through rocks of normal crustal density. The T gradient, dT/dz, was estimated to be −100°/km, the difference between 595 °C and a surface T of 25 °C divided by the inferred depth of metamorphism in the area (5.6 km). The relationship between q and z specified by Eq. 5 was then computed by fitting values of $(1 - X_{CO_2})/(X_{CO_2} - X^{\circ}_{CO_2})$ along the flow path to a second order polynomial in z with X_{CO_2} defined by the Cal-Qtz-Wo equilibrium (assuming $p_{CO_2} + p_{H_2O} = P_{total}$), integrating the polynomial with respect to z, and evaluating the integral between 0 and z.

With these input values, Eqs. 4 and 5 predict that infiltration would have produced a Wo-reaction front that moved faster than the O-isotope alteration front. The upward limit of the Wo-reaction front is at 3090 m elevation (Fig. 2). Corrected for the effects of devolatilization, the O-isotopic compositions of analyzed Wo-bearing limestone from location 4 (the lowest elevation sampled) are not significantly different from the compositions of Wo-free limestone elsewhere in the study area (Table 3; Fig. 9B). The upper limit of the O-isotope alteration front therefore lies buried below 3010 m. A lower bound on the time-integrated flux of prograde metamorphism associated with Reaction 1 is the value of q that would produce a separation of 80 m between the faster-moving Wo-reaction front and the slower-moving, O-isotope alteration front. The lower bound on q is 245 mol fluid/cm^2 rock. The associated value of z is 101 m, corresponding to a maximum elevation of the inlet to the flow system of ≈ 2989 m (101 m below the upper limit of Wo). The inferred depth to the inlet of the flow system below the carbonate layer is consistent with a magmatic fluid source, considering the nearby exposure of granodiorite around the NE side of Thousand Island Lake at 3000 m elevation (Figs. 2, 12). The calculated depth to the inlet, however, does not rule out dehydrating metavolcanic rocks as a fluid source. A lower bound on prograde time-integrated fluid flux was computed for each analyzed Wo-bearing specimen from Eq. 5 taking z as the difference between the elevation of each sample location and 2989 m and assuming that the mineralogy of rock along the fluid flow path beneath is identical to that in the sample collected at the surface. The range of lower bounds is 20 to 390 mol/cm^2 (Figs. 3–7). The overall range of values reflects both different elevations of the sample localities and the range of measured reaction capacity, $\xi_{\max}$, in individual samples (defined, in turn, by bulk rock composition).

The greatest distance that the Wo-reaction front could have traveled upward during prograde contact metamorphism is the difference in elevation between the upper limit of the front, 3090 m (Fig. 2), and the point at depth where Cal, Qtz, and Wo would have been in equilibrium with pure CO_2. Using preferred values for peak P and T at location 2 and for gradients in P and T along the inferred flow path, that point lies 1160 m below location 2. An upper bound on the time-integrated flux associated with Wo-formation was then estimated by applying Eq. 5, setting $z = 1160$ m, and values of other input variables as specified above. The upper bound on q is 1615 mol/cm^2. An upper bound on prograde time-integrated fluid flux was computed for each analyzed Wo-bearing specimen assuming that the mineralogy of rock along the fluid flow path beneath is identical to that in the sample collected at the surface. The range of upper bounds is 560 to 3210 mol/cm^2 (Figs. 3–7). The overall range of values corresponds to the range of measured reaction capacity, $\xi_{\max}$, in individual samples.

Retrograde fluid flow

Geometry of flow

Retrograde carbonation and hydration reactions produced Tr by Reaction 3 and Qtz by the reverse of Reaction 1. Both types of reactions inevitably are driven by chemical equilibrium between rock and fluid flowing in the direction of decreasing T (Baumgartner and Ferry 1991; Ferry and Dipple 1991). In the study area, down-T flow could have occurred during retrograde metamorphism if flow was either upward or horizontal and directed away from the exposure of granodiorite at Thousand Island Lake. Upward retrograde fluid flow is more appealing because no change in flow geometry would be required during transition between the conditions of prograde and retrograde metamorphism. Layer-parallel retrograde flow is indicated by the spatial distribution of calculated values of retrograde time-integrated flux (see below).

Estimates of the amount of retrograde fluid flow

The ubiquitous presence of both reactants and products of retrograde Reactions 1 and 3 in the study area implies that the reactions were driven by pervasive down-T flow of CO_2-H_2O fluid through the siliceous carbonate rocks under conditions where local mineral-fluid equilibrium was attained or closely approached (Ferry 1996a). Flow and reaction occurred over some interval in T between the peak value (T_{pk}) and the final T at which flow ceased (T_f). Quantitative estimation of time-integrated flux (q) therefore requires some explicit coupling between T and q. Following Ferry (1996a), fluid flux was assumed to be proportional to cooling rate (i.e., dq/dT = constant), a relationship based on the plausible assumption that the aureole was infiltrated continuously as it cooled between T_{pk} and T_f. The relationship between progress (ξ) of a reaction involving carbonation and/or hydration driven by fluid flow along a P and/or T gradient and molar time-integrated flux then is:

$$\xi = q\overline{A} \tag{6}$$

where

$$\overline{A} = \frac{\int_{T_f}^{T_{pk}} A(T)\,dT}{T_{pk} - T_f}, \tag{7}$$

$$A = \frac{(\partial X_{CO_2}/\partial T)_P (dT/dz) + (\partial X_{CO_2}/\partial P)_T (dP/dz)}{\nu_{CO_2} - X_{CO_2}(\nu_{CO_2} + \nu_{H_2O})}, \tag{8}$$

$(\partial X_{CO_2}/\partial T)_P$ and $(\partial X_{CO_2}/\partial P)_T$ are the T- and P-dependence of fluid composition at the reaction site, and ν_{CO_2} and ν_{H_2O} are the stoichiometric coefficients of CO_2 and H_2O in the reaction (Baumgartner and Ferry 1991; Ferry 1996a). The time-integrated flux of retrograde fluid flow in Wo-bearing siliceous limestone and calc-silicate hornfels was estimated by applying Eqs. 6–8 to formation of Cal and Qtz by the reverse of Reaction 1. Because all Qtz in Wo-bearing rocks appears to have formed by Reaction 1 in reverse (Figs. 8B, C), reaction progress was taken as the amount of Qtz in each sample. Values of X_{CO_2}, $(\partial X_{CO_2}/\partial T)_P$, and $(\partial X_{CO_2}/\partial P)_T$ were computed from the mineral-fluid equilibrium corresponding to Reaction 1. The P- and T-gradients along the flow path were considered the same as those specified above. The minor development of Srp and the preservation of abundant Fo in siliceous dolomite at locations 2 and 4 indicate that retrograde fluid flow in the dolomite occurred at but not significantly below T of the Fo-Brc-Dol-Cal-Srp-fluid isobaric invariant point at 1500 bars (375 °C). The minor development of Czo + Qtz and the preservation of unreacted An-Grs contacts in siliceous limestone and hornfels indicate that retrograde fluid flow in limestone and hornfels occurred at but not significantly below T of the An-Grs-Czo-Qtz-H_2O isobaric invariant point at 1500 bars (420 °C). Accordingly, T_{pk} was taken as 595 °C and T_f, somewhat arbitrarily, as 400 °C. Calculations estimate the time-integrated flux associated with coupled fluid flow and formation of Qtz + Cal by the reverse of Reaction 1 at T-X_{CO_2} conditions along the solid shaded curve in Fig. 11 with decreasing T. Calculated values of retrograde q in 13 analyzed Wo-bearing rocks fall in the range 0 to 1770 mol/cm^2, averaging $\approx$ 500 mol/cm^2 (Table 4B).

The progress of Reaction 3 should record the retrograde time-integrated flux in Wo-free limestone and hornfels. Reaction 3 initiated in Wo-free rocks at some T below the T maximum of the Tr-Cal-Qtz-Di-fluid equilibrium (515–530 °C). Without better constraints on the T at which Tr first formed, the potential for Reaction 3 quantitatively to record q cannot be realized.

Dependence of calculated time-integrated flux on input data and assumptions

The uncertainties in estimated peak P and T in the study area (±500 bars, ±25 °C) introduce uncertainties in calculated q of a factor of $\approx$2 or less (Table 4). Infiltration of siliceous limestone and prograde formation of Wo could have started at a T below the peak value. The development of both Wo by Reaction 1 and Grs by Reaction 2 at the mineral reaction front, however, requires that infiltration began at T above the Grs-Qtz-An-Wo equilibrium (Fig. 11; 550–560 °C at 1500 bars). If infiltration was continuous as the aureole heated from 550 to 595 °C, the bounds on the prograde time-integrated flux would approximately correspond to those in Table 4A computed for peak T = 570 °C. In the case of a prograde infiltration-driven reaction at T = 550–595 °C, time-integrated flux would be a factor of $\approx$2 greater than the preferred value in Table 4A. Lower bounds on prograde time-integrated flux are almost independent of the assumed T gradient along the flow path because values of z are small. Upper bounds on prograde q and calculated values of retrograde q scale approximately with the inverse of the T gradient along the flow path. If dT/dz was,

Table 4 Estimated time-integrated fluid flux. Values of time-integrated flux (q) in mol fluid/cm^2 rock. z refers to the distance the Wo-reaction front traveled upward to present level of exposure. *Lower bound* refers to q required to develop a separation of 80 m between the Wo-reaction and O-isotope alteration fronts. *Upper bound* refers to q if the Wo-reaction front rose from a point at depth where Cal + Qtz + Wo were in equilibrium with pure CO_2

A Prograde metamorphism

Model	Lower bound		Upper bound	
	z (m)	q (mol/cm^2)	z (m)	q (mol/cm^2)
Baseline[a]	101	245	1160	1615
+25 °C[b]	90	150	855	970
−25 °C[c]	129	500	1465	2630
+500 bars[d]	135	550	1530	2820
−500 bars[e]	87	120	700	725
200°/km[f]	98	220	520	730
50°/km[g]	103	260	2915	4050
Maximum Wo[h]	133	630	1160	3215
Minimum Wo[i]	86	75	1160	555

B Retrograde metamorphism

Model/sample	2D	2H	2O	3B	3D	3F	3N	3O	4B	4D	4E	4G	4I
Baseline[j]	1190	500	1060	560	60	90	420	280	280	20	210	1770	0
+25 °C[b]	740	310	660	350	40	60	260	180	170	10	130	1100	0
−25 °C[c]	1860	780	1650	880	100	150	660	450	440	30	320	2770	0
+500 bars[d]	2160	900	1920	1020	120	170	770	520	510	30	370	3220	0
−500 bars[e]	560	240	500	270	30	40	200	140	130	10	100	840	0
200°/km[f]	550	230	490	260	30	40	190	130	130	10	100	820	0
50°/km[g]	2930	1230	2600	1380	160	230	1040	700	690	40	510	4360	0
$+\sigma_{Qtz}$[k]	1330	590	1180	660	100	130	500	350	350	30	260	1940	0
$-\sigma_{Qtz}$[l]	1060	410	930	470	30	60	340	220	210	0	150	1610	0

[a] Preferred model based on peak T = 595 °C, P = 1500 bars at present level of exposure; vertical flow; $dT/dz = -100$/km; ξ_{max} in Eq. 5 = $7.4 \cdot 10^{-3}$ mol/cm^3

[b] Values if peak T at present level of exposure was 25 °C greater than assumed

[c] Values if peak T at present level of exposure was 25 °C less than assumed

[d] Values if peak P at present level of exposure was 500 bars greater than assumed

[e] Values if peak P at present level of exposure was 500 bars less than assumed

[f] Values if dT/dz was −200°/km along the flow path

[g] Values if dT/dz was −50°/km along the flow path

[h] Values if ξ_{max} in Eq. 5 was the largest measured ($14.717 \cdot 10^{-3}$ mol/cm^3, sample 3O)

[i] Values if ξ_{max} in Eq. 5 was the smallest measured ($2.553 \cdot 10^{-3}$ mol/cm^3, sample 4G)

[j] Preferred model based on peak T = 595 °C, P = 1500 bars at present level of exposure; vertical flow; $dT/dz = -100$/km; ξ for Reaction 1 measured as described in text; continuous flow and reaction at local mineral-fluid equilibrium between 595 and 400 °C; fluid flux proportional to cooling rate

[k] Values if Qtz contents were one standard deviation greater than measured, from point counting statistics (Chayes 1956)

[l] Values if Qtz contents were one standard deviation less than measured

for example, −50°/km or −200°/km, q would increase or decrease, respectively, by a factor of ≈ 2. The preferred estimate of prograde time-integrated flux is based on the average Wo and Grs contents inferred for Wo-bearing limestone and hornfels at the peak of metamorphism. If the Wo and Grs contents of the carbonate layer were everywhere as high as those of the sample with the most (sample 3O, Table 1), calculated prograde q would increase by a factor of ≈ 2. If the Wo and Grs contents of the carbonate layer were everywhere as low as those of the sample with the least (sample 4G, Table 1), computed q would decrease by a factor of ≈ 3. Estimates of retrograde time-integrated flux are based on the modal abundance of Qtz in individual samples. An uncertainty in modal Qtz equivalent to one standard deviation based on point counting statistics typically introduces an uncertainty in calculated q of a factor of 50% relative or less.

The preferred model for coupled retrograde fluid flow and mineral reaction in Wo-bearing rocks is continuous flow of fluid through rocks at local mineral-fluid equilibrium with flux proportional to cooling rate. Input fluids could not have been richer in H_2O than the equilibrium composition because they then could not drive a carbonation reaction, such as Reaction 1 in reverse. Infiltration by fluids richer in CO_2 than equilibrium values would produce a carbonation front separating completely carbonated rocks upstream from less carbonated rocks downstream, a feature not observed at the present level of exposure. Even if such a carbonation front is concealed at depth, our model is appropriate for inverting measured reaction progress to obtain values of retrograde time-integrated flux. If retrograde fluid flux was not proportional to cooling rate, values of retrograde time-integrated flux would differ from those in Table 4B. For more flow at high T than low T, time-integrated flux would be less. If

there was more flow at low T than high T, time-integrated flux would be greater. In the extreme cases of all retrograde fluid flow at 595 °C or 400 °C, calculated values of q in Table 4B would decrease by a factor of 5 or increase by a factor of 25, respectively.

Discussion

Structural control on the geometry of contact metamorphic fluid flow

Transport theory predicts that infiltration of homogeneous rock with an isotropic permeability structure by chemically reactive fluid across a planar inlet will produce a planar reaction front that propagates along the flow path (in the absence of significant diffusion and dispersion). The distribution of Wo-bearing rocks in the study area dramatically fails to meet this prediction. The Wo-reaction front has fingers that extend 20–30 m parallel to the inferred direction of flow (Figs. 3–6, 12). The farthest advance of the Wo-reaction front is at contacts between limestone and more siliceous rock, either calc-silicate hornfels or metavolcanic rock (Figs. 4–5). The fingers do not likely result from volatile transport across these contacts, either by diffusion or advection. If that were the case, specimens like sample 3B, that lies 0.2 m from the contact between limestone and metavolcanic rock in a layer of Wo-bearing rock 4.3 m wide (Fig. 5), should exhibit O-isotope alteration. Furthermore, fingers like the northeastern layer of Wo-bearing rock at location 2 (Fig. 4) cannot be explained by cross-layer volatile transport because the mineral assemblage in rocks on either side of the finger is identical and the same as that inferred for the finger prior to initiation of prograde Reaction 1. Evidently the lithologic contacts were zones of elevated permeability that favored fluid access parallel to the contact. The distribution of Wo-bearing rocks illustrates a significant focusing of contact metamorphic fluid flow by premetamorphic structures. Structural control of fluid flow is well documented in other aureoles with cases of enhanced flow along bedding (Nabelek et al. 1984; Jamtveit et al. 1992; Bowman et al. 1994; Heinrich and Gottschalk 1994; Ferry and Rumble 1997), breccia zones (Ferry 1995b), and contacts between metasedimentary and premetamorphic intrusive rocks (Gerdes et al. 1995b; Ferry and Rumble 1997).

Centimeter-sized Wo grains at locations 2 and 3 are boudinaged in the plane of lithologic layering, which indicates that prograde metamorphic fluid flow began when penetrative deformation was still active. Numerous other studies have documented a temporal relationship between active deformation and metamorphic fluid flow (Oliver 1996). Deformation may play a vital role in activating premetamorphic structures for enhanced metamorphic fluid flow. No interconnected grain boundary porosity network exists to accommodate fluid flow under most static P-T-fluid composition conditions of metamorphism (Holness and Graham 1995). Active deformation may be one means of creating a grain-scale permeability network. Deformation-enhanced permeability will be greatest at the contact between rocks with disparate mechanical properties, for example along contacts between different sedimentary rocks types (as in the study area) or between sedimentary and igneous rocks (this study, Oliver 1996).

Distribution and significance of retrograde fluid flow

Calculated values of retrograde time-integrated flux differ significantly between samples collected from various layers at locations 2, 3, and 4 (Table 4B). The spatial distributions of calculated retrograde q at each location rules out a significant cross-layer component of pervasive retrograde fluid flow associated with the reverse of Reaction 1. Pervasive retrograde flow, like prograde flow, apparently was parallel to lithologic layering. Quartz veins in the area demonstrate that some retrograde fracture-controlled fluid flow, however, cut across layering (Hanson et al. 1993).

The estimated time-integrated fluid flux of retrograde metamorphism is comparable to the prograde time-integrated flux (Table 4). As is emerging from the study of aureoles worldwide (e.g., Ferry 1996a; Ferry and Rumble 1997), the quantity of fluid that flows pervasively through the inner parts of aureoles as they cool is as large as if not greater than the amount of fluid that flows through them near the peak of metamorphism. Thus mineralogical studies will accurately characterize the entire fluid flow history of an aureole only if both prograde and retrograde mineral reactions are explicitly considered. The importance of retrograde mineral-fluid reactions in recording contact metamorphic fluid flow could have been foreseen from thermal-hydrologic models that predict significant quantities of fluid flow through the inner parts of a contact aureole following its thermal maximum (Norton and Knight 1977; Hanson 1992, 1995a).

Petrologic and isotopic constraints on fluid flow during contact metamorphism

Two approaches are used to estimate the geometry and amount of fluid flow during contact metamorphism: (1) integrated thermal and hydrologic models of fluid flow around a hot pluton (e.g., Norton and Knight 1977; Hanson 1992, 1995a; Gerdes et al. 1995a); (2) application of the mass continuity equation to the distribution of minerals and isotopic compositions in contact aureoles (e.g., Bickle and McKenzie 1987; Ferry 1991; Bowman et al. 1994; Dipple and Ferry 1996). Numerical simulations of heat and fluid transport and quantitative interpretation of oxygen isotope data have led to internally consistent models for fluid flow in the Skaergaard hydrothermal system (Norton and Taylor 1979; Manning et al. 1993). Nevertheless, the reliability of estimates

of fluid flow geometry and amount based on some applications of the mass continuity equation has recently been questioned (Hanson 1995b; Cartwright and Buick 1996; Holness and Fallick 1997). A comparison of results of this study with predictions made by the numerical model for contact metamorphic fluid flow in the Ritter Range pendant by Hanson et al. (1993) therefore is revealing.

A meaningful comparison between the results of this study and predictions made by the model of Hanson et al. (1993) is predicated on the assumption that conclusions about fluid flow based on study of the carbonate layer can be extrapolated to the larger exposure of metamorphic rocks in the area of Fig. 1 that the numerical model simulated. Because metavolcanic rocks of the Ritter Range do not contain the same kind of isotopic or mineralogical records of prograde metamorphic fluid flow considered in this study, it cannot be determined whether the history of prograde fluid flow in the carbonate layer matches that of surrounding rocks. The metavolcanic rocks, however, contain abundant retrograde muscovite, chlorite, margarite, and tourmaline, especially at grades higher than the And + Kfs isograd (Hanson et al. 1993), implying that the pervasive, down-T retrograde fluid flow that affected the carbonate layer was experienced by much or all of the area in Fig. 1. In addition, meaningful comparison of the thermal-hydrologic model with interpretation of the isotopic and mineralogical data requires that the driving forces for fluid flow in the numerical simulation were also the primary ones that drove fluid flow during contact metamorphism in the Ritter Range pendant.

In spite of some uncertainty in the validity of the two assumptions that underlie the comparison, the agreement between predictions of the geometry and amount of flow during contact metamorphism of the Ritter Range pendant, made by interpretation of stable isotope and mineralogical data (this study) and independently made by the thermal-hydrologic model (Hanson et al. 1993), is excellent. The physical model predicts that metamorphic fluid flow within ≈ 1 km of the granodiorite was vertical and upward, the same flow geometry deduced from interpreting the spatial distribution of Wo-bearing and Wo-free limestone with transport theory. The numerical model preferred by Hanson et al. (1993) for a permeability of 1 μD predicts that time-integrated flux was $\approx 4.5 \cdot 10^5$ kg/m^2 at the present level of exposure with an uncertainty of a factor of ≈ 2 or more. The total time-integrated fluid flux of contact metamorphism recorded by mineral reaction progress in Wo-bearing rocks is the sum of that recorded by the prograde Wo-forming reaction (245–1615 mol/cm^2, Table 4A) and the estimated time-integrated flux of retrograde fluid flow recorded by the reverse of Reaction 1 ($\approx$ 200–1000 mol/cm^2, Table 4B). Considering that the model input fluid which drove Reactions 1 and 2 is pure H_2O, that the volatiles produced along the flow path by prograde reaction were pure CO_2, and that the retrograde fluid can be approximated for the purposes of this calculation by H_2O, the range in total molar time-integrated flux of contact metamorphism, 445–2615 mol/cm^2, corresponds to a range in mass flux of 1–6 $\cdot 10^5$ kg/m^2. The estimate from the numerical model, $4.5 \cdot 10^5$ kg/m^2, falls within the range of values predicted from the mineralogical and isotopic record.

Petrologic data of this study validate two other important aspects of the numerical model. First, the lower limit on p_{CO_2} required to stabilize Dol + Di in siliceous dolomite (1440 bars) and the upper limit on P_{total} of 2000 bars means that $P_{fluid} > 0.72P_{total}$, supporting preferred values of permeability during prograde metamorphism in the thermal-hydrologic model (0.1–1 μD) that result in $P_{fluid} \approx P_{total}$. Second, the observed geometry of fingering of the Wo-reaction front (Fig. 12) indicates that permeability at the peak of metamorphism was greater in the vertical direction than in the horizontal (Lichtner 1996), verifying the assumption in the numerical model that permeability in the vertical direction was greater than in the horizontal in that part of the model that represents the area in Fig. 1.

This study identifies two factors that, at least in part, may explain prior disagreement between studies of contact metamorphic fluid flow based on thermal and hydrologic models and those based on petrology and geochemistry. First, post-peak fluid flow in the study area drove hydration and/or carbonation reactions that converted peak isobaric divariant (or higher variance) mineral assemblages into isobaric univariant assemblages during retrograde metamorphism (e.g., Cal-Qtz-Wo in Wo-bearing rocks and Tr-Cal-Qtz-Di in Wo-free limestone and hornfels). If the widespread assemblages Cal-Qtz-Wo and Tr-Cal-Qtz-Di were mistakenly considered prograde, the inferred geometry of prograde fluid flow incorrectly would have been in the direction of increasing rather than decreasing T (Ferry 1991). Erroneous predictions of the direction of contact metamorphic fluid flow can result from incorrectly interpreting a retrograde mineral assemblage that formed as the aureole cooled as a prograde assemblage formed as the aureole heated.

Second, structural control of contact metamorphic fluid flow can cause ambiguous interpretations of the mineralogical and isotopic records of the amount and direction of fluid flow. Applications of the mass continuity equation to the distribution of minerals in contact aureoles typically assume that an aureole is initially isotropic in its physical, chemical, and mineralogical properties on the scale at which samples are collected. Unless sampling is conducted at a scale commensurate with that of the smallest significant lithologic or structural heterogeneities, interpretation of contact metamorphic fluid flow may err. For example, if only samples 1H, 2N, 3L, and 4G (Table 1) had been collected and if tiny Wo inclusions in Qtz in sample 4G were overlooked, an absence of metamorphic infiltration would erroneously have been inferred for the entire carbonate layer. Alternatively, if only samples 2H, 3B, and 4D (Table 1) had been collected, metamorphic fluid flow

might erroneously have been considered pervasive in the entire carbonate layer. Likewise, numerical studies that assume isotropic rock properties or neglect possible structural controls of fluid flow at the 0.1 to 100 m scale may fail correctly to predict fundamental aspects of contact metamorphic fluid flow (cf. Cook et al. 1997). The mineralogical record of metamorphism is a powerful tool for overcoming this potential problem. Under favorable circumstances, the distribution of minerals like Wo can image metamorphic fluid flow paths in the field. The smallest lithologic or structural heterogeneities controlling the geometry of flow then can be observed directly and samples collected for petrologic studies or grid-spacing selected for numerical models at the appropriate scale.

Both careful, site-specific thermal-hydrologic modeling and interpretation of mineralogy and isotope geochemistry can produce mutually consistent predictions about fluid flow during contact metamorphism in individual aureoles. The two approaches are complementary and together provide a deeper understanding of metamorphic processes than can be obtained from either method by itself.

Acknowledgments We thank Brooks Hanson, Tom Hoisch, and Craig Manning for thoughtful reviews and Victoria Avery, Barbara Dutrow and Mario Giaramita for assistance with field work. Research was supported by grant EAR-9404578 from the National Science Foundation to J.M.F and by the Sprague and Becker Funds of the Smithsonian Institution to S.S.S.

References

Anovitz LM, Essene EJ (1987) Phase equilibria in the system $CaCO_3$-$MgCO_3$-$FeCO_3$. J Petrol 19: 389–414

Armstrong JT (1988) Quantitative analysis of silicate and oxide minerals: comparison of Monte Carlo, ZAF and phi-rho-z procedures. In: Newbury DE (ed) Microbeam analysis – 1988. San Francisco Press, San Francisco, pp 239–246

Baumgartner LP, Ferry JM (1991) A model for coupled fluid-flow and mixed-volatile mineral reactions with applications to regional metamorphism. Contrib Mineral Petrol 106: 273–285

Berman RG (1988) Internally consistent thermodynamic data for minerals in the system Na_2O–K_2O-CaO-MgO-FeO-Fe_2O_3-Al_2O_3-SiO_2-TiO_2-H_2O-CO_2. J Petrol 29: 445–522

Bickle MJ, McKenzie DM (1987) The transport of heat and matter by fluids during metamorphism. Contrib Mineral Petrol 95: 78–93

Bowman JR, Willett SD, Cook SJ (1994) Oxygen isotopic transport and exchange during fluid flow: one-dimensional models and applications. Am J Sci 294: 1–55

Cartwright I, Buick IS (1996) Determining the direction of contact metamorphic fluid flow: an assessment of mineralogical and stable isotope criteria. J Metamorphic Geol 14: 289–305

Chayes F (1956) Petrographic modal analysis: an elementary statistical appraisal. John Wiley, New York

Cook SJ, Bowman JR, Forster CB (1997) Contact metamorphism surrounding the Alta stock: finite element model simulation of heat- and $^{18}O/^{16}O$ mass-transport during prograde metamorphism. Am J Sci 297: 1–55

Coplen TB (1988) Normalization of oxygen and hydrogen isotope data. Chem Geol 72: 293–297

Coplen TB (1996) New guidelines for reporting stable hydrogen, carbon, and oxygen isotope-ratio data. Geochim Cosmochim Acta 60: 3359–3360

Dipple GM, Ferry JM (1992) Fluid flow and stable isotopic alteration of rocks at elevated temperatures with applications to metamorphism. Geochim Cosmochim Acta 56: 3539–3550

Dipple GM, Ferry JM (1996) The effect of thermal history on the development of mineral assemblages during infiltration-driven contact metamorphism. Contrib Mineral Petrol 124: 334–345

Ferry JM (1991) Dehydration and decarbonation reactions as a record of fluid infiltration. In: Kerrick DM (ed) Contact metamorphism. (Reviews in mineralogy, vol. 26) Mineral Soc Am, Washington, DC, pp 351–393

Ferry JM (1994) Overview of the petrologic record of fluid flow during regional metamorphism in northern New England. Am J Sci 294: 905–988

Ferry JM (1995a) Role of fluid flow in the contact metamorphism of siliceous dolomitic limestones – reply to Hanson. Am Mineral 80: 1226–1228

Ferry JM (1995b) Fluid flow during contact metamorphism of ophicarbonate rocks in the Bergell aureole, Val Malenco, Italian Alps. J Petrol 36: 1039–1053

Ferry JM (1996a) Prograde and retrograde fluid flow during contact metamorphism of siliceous carbonate rocks from the Ballachulish aureole, Scotland. Contrib Mineral Petrol 124: 235–254

Ferry JM (1996b) Three novel isograds in metamorphosed siliceous dolomites from the Ballachulish aureole, Scotland. Am Mineral 81: 485–494

Ferry JM, Dipple GM (1991) Fluid flow, mineral reactions, and metasomatism. Geology 19: 211–214

Ferry JM, Rumble D (1997) Formation and destruction of periclase by fluid flow in two contact aureoles. Contrib Mineral Petrol 128: 313–334

Fiske RS, Tobisch OT (1978) Paleogeographic significance of volcanic rocks of the Ritter Range pendant, central Sierra Nevada, California. In: Howell DG, McDougall KA (eds) Mesozoic paleogeography of the western United States. (Pacific coast paleogeography symposium, vol 2) Soc Econ Paleontol Mineral Pac Sect Los Angeles, pp 209–219

Gerdes ML, Baumgartner LP, Person M (1995a) Stochastic permeability models of fluid flow during contact metamorphism. Geology 23: 945–948

Gerdes ML, Baumgartner LP, Person M, Rumble D (1995b) One and two dimensional models of fluid flow and stable isotope exchange at an outcrop in the Adamello contact aureole, Southern Alps, Italy. Am Mineral 80: 1004–1019

Hanson RB (1992) Effects of fluid production on fluid flow during regional and contact metamorphism. J Metamorphic Geol 10: 87–97

Hanson RB (1995a) The hydrodynamics of contact metamorphism. Geol Soc Am Bull 107: 595–611

Hanson RB (1995b) Role of fluid flow in the contact metamorphism of siliceous dolomitic limestones – discussion. Am Mineral 80: 1222–1225

Hanson RB, Sorensen SS, Barton MD, Fiske RS (1993) Long-term evolution of fluid-rock interactions in magmatic arcs: evidence from the Ritter Range pendant, Sierra Nevada, California, and numerical modeling. J Petrol 34: 23–62

Heinrich W, Gottschalk M (1994) Fluid flow patterns and infiltration isograds in melilite marbles from the Bufa del Diente contact metamorphic aureole, north-east Mexico. J Metamorphic Geol 12: 345–359

Holland TJB, Powell R (1990) An enlarged and updated internally consistent thermodynamic dataset with uncertainties and correlations: the system K_2O-Na_2O-CaO-MgO-MnO-FeO-Fe_2O_3-Al_2O_3-SiO_2-TiO_2-C-H_2-O_2. J Metamorphic Geol 8: 89–124

Holness MB, Fallick AE (1997) Palaeohydrology of the calc-silicate aureole of the Beinn an Dubhaich granite, Skye, Scotland: a stable isotope study. J Metamorphic Geol 15: 71–83

Holness MB, Graham CM (1995) *P-T-X* effects on equilibrium carbonate H_2O-CO_2-NaCl dihedral angles: constraints on carbonate permeability and the role of deformation during fluid infiltration. Contrib Mineral Petrol 119: 301–313

Jamtveit B, Grorud HF, Bucher-Nurminen K (1992) Contact metamorphism of layered carbonate-shale sequences in the Oslo Rift. II. Migration of isotopic and reaction fronts around cooling plutons. Earth Planet Sci Lett 114: 131–148

Kerrick DM, Jacobs GK (1981) A modified Redlich-Kwong equation for H_2O, CO_2, and H_2O-CO_2 mixtures at elevated pressures and temperatures. Am J Sci 281: 735–767

Kohn MJ, Valley JW (1994) Oxygen isotope constraints on metamorphic fluid flow, Townshend Dam, Vermont, USA. Geochim Cosmochim Acta 58: 5551–5566

Kretz R (1983) Symbols for rock-forming minerals. Am Mineral 68: 277–279

Labotka TC, Nabelek PI, Papike JJ (1988) Fluid infiltration through the Big Horse Limestone Member in the Notch Peak contact-metamorphic aureole, Utah. Am Mineral 73: 1302–1324

Lichtner PC (1996) Continuum formulation of multicomponent-multiphase reactive transport. In: Lichtner PC, Steefel CI, Oelkers EH (eds) Reactive transport in porous media. (Reviews in mineralogy, vol 34) Mineral Soc Am, Washington, DC, pp 1–81

Manning CE, Ingebritsen SE, Bird DK (1993) Missing mineral zones in contact metamorphosed basalts. Am J Sci 293: 894–938

McCrea JM (1950) On the isotopic chemistry of carbonates and a paleotemperature scale. J Chem Phys 18: 849–857

Nabelek PI (1991) Stable isotope monitors. In: Kerrick DM (ed) Contact metamorphism. (Reviews in mineralogy, vol 26). Mineral Soc Am, Washington, DC, pp 395–436

Nabelek PI, Labotka TC, O'Neil JR, Papike JJ (1984) Contrasting fluid/rock interaction between the Notch Peak granitic intrusion and argillites and limestones in western Utah: evidence from stable isotopes and phase assemblages. Contrib Mineral Petrol 86: 25–34

Norton D, Knight J (1977) Transport phenomena in hydrothermal systems: cooling plutons. Am J Sci 277: 937–981

Norton D, Taylor HP Jr (1979) Quantitative simulation of the hydrothermal systems of crystallizing magmas on the basis of transport theory and oxygen isotope data: an analysis of the Skaergaard intrusion. J Petrol 20: 421–486

Oliver NHS (1996) Review and classification of structural controls on fluid flow during regional metamorphism. J Metamorphic Geol 14: 477–492

Rumble D, Oliver NHS, Ferry JM, Hoering TC (1991) Carbon and oxygen isotope geochemistry of chlorite-zone rocks of the Waterville limestone, Maine, U.S.A. Am Mineral 76: 857–866

Skelton ADL (1996) The timing and direction of fluid flow in Vermont. Contrib Mineral Petrol 125: 75–84

Skippen GB (1974) An experimental model for low pressure metamorphism of siliceous dolomitic marble. Am J Sci 274: 487–509

Sorensen SS, Dunne GC, Hanson RB, Barton MD, Becker J, Tobisch OT, Fiske RS (1998) From Jurassic shores to Cretaceous plutons: geochemical evidence for paleo-alteration environments of metavolcanics rocks, eastern California. Geol Soc Am Bull 110 (in press)

Stern TW, Bateman PC, Morgan BA, Newell MF, Peck DL (1981) Isotopic U-Pb ages of zircon from the granitoids of the central Sierra Nevada, California. US Geol Surv Prof Pap 1185

Swart PK, Burns SJ, Leder JJ (1991) Fractionation of the stable isotopes of oxygen and carbon in carbon dioxide during the reaction of calcite with phosphoric acid as a function of temperature and technique. Chem Geol 86: 89–96

Tobisch OT, Fiske RS (1982) Repeated parallel deformation in part of the Sierra Nevada, California, and its implications for dating structural events. J Struct Geol 4: 177–195

Tobisch OT, Sacks S, Taniguchi D (1977) Strain in metamorphosed volcaniclastic rocks and its bearing on the evolution of orogenic belts. Geol Soc Am Bull 88: 23–40

Valley JW (1986) Stable isotope geochemistry of metamorphic rocks. In: Valley JW, Taylor HP Jr, O'Neil JR (eds) Stable isotopes in high temperature geological processes. (Reviews in mineralogy, vol 16) Mineralogical Soc Am, Washington, DC, pp 445–489

Walther JV, Orville PM (1982) Volatile production and transport in regional metamorphism. Contrib Mineral Petrol 79: 252–257